

A design report submitted to the Faculty of Engineering and the Built Environment, University of the Witwatersrand, Johannesburg, in partial fulfilment of the requirements for the degree of Bachelor of Science in Engineering.



## **Disclosure – Use of Artificial-Intelligence (AI) Generated Content - 2024 V2**

### ***1. Disclosure: Editing/refining***

☒ We acknowledge the use of ChatGPT 3.5, April (<https://chatgpt.com/>) to improve the flow and readability of the various paragraphs within our assignment. We uploaded the text for our MECN4029 Assignment, and we entered the following prompts:

Original prompt: "Refine the grammar and flow of the following paragraphs"

\*This prompt was used in multiple instances within the compilation of the current report\*

The output from these prompts was used to correct the grammar and the flow of the paragraphs.

☒ ***We declare that the disclosure is complete and truthful.***

Student number: 2426865, 2445065, 2440136, 2424362

Course code: MECN4029

Date: 2024/05/20

## EXECUTIVE SUMMARY

This report details the development and analysis of a sun tracking solar farm for an old age home in Upington, addressing the challenge of six hours of daily load shedding. The project aimed to optimize solar energy capture by enabling solar panels to follow the sun's movement, thereby maximizing power generation.

The development process included the creation of a mathematical model incorporating Newton's Second Law and Kirchhoff's Voltage Law for an armature-controlled DC motor, a gear system, and the solar panel dynamics. Wind effects were included and subsequently linearized to facilitate analytical analysis. A thorough stability analysis was performed on the linearized transfer function using Nyquist and Bode criteria, and the stability of the non-linear model was verified by definition. The system demonstrated absolute and BIBO (Bounded Input, Bounded Output) stability, although it exhibited sluggish responses and significant steady-state error.

To address these performance issues, a controller was designed using both PID and root locus techniques. The goal was to achieve a responsive yet not overly aggressive control system, minimizing susceptibility to both noise and steady-state error. The resulting controller effectively tracked steady changes in sun position but faced challenges with large, sudden changes due to the absence of dedicated damping mechanisms, relying solely on motor damping and wind drag.

Despite these challenges, the solar tracker met the power requirements of the old age home during winter days and fit within the spatial constraints of the facility. This requires 114 solar panels, which generate 0.8001 kWh each on the winter solstice and 1.2689 kWh each during the summer solstice. The successful implementation of the sun tracking system demonstrated its viability and effectiveness in a scenario where a fixed-tilt solar farm was inadequate. Overall, the project achieved its objective of enhancing energy reliability for the old age home amidst frequent power outages.

# TABLE OF CONTENTS

Executive Summary .....	i
List of Figures .....	iv
List of Tables .....	v
Nomenclature.....	vi
1 Introduction .....	1
1.1 Environmental Factors .....	2
1.2 Scenario Development .....	2
1.3 Problem Summary .....	4
2 System Design and Modelling.....	5
2.1 Sun Positioning and Types of Solar Tracking .....	5
2.2 Non-linear Model Development .....	7
2.2.1 Design Decisions.....	7
2.2.2 Assumptions .....	9
2.2.3 Model Formulation.....	9
2.2.4 Simulink Representation .....	11
2.3 Model Linearisation .....	12
2.3.1 Operating point.....	12
2.3.2 Linearisation.....	13
2.3.3 Transfer Function .....	14
2.3.4 System Specifications .....	14
2.3.5 Linearisation Validation.....	16
2.3.6 Linear Simulink Model .....	16
3 System Analysis .....	17
3.1 Stability Analysis .....	17
3.1.1 Linear stability analysis.....	17
3.1.2 Non-linear stability analysis.....	22
3.1.3 Comparison of non-linear vs linear performance.....	24
3.1.4 Control Implication .....	25

4	Controller Implementation.....	27
4.1	Closed Loop Controller Design .....	27
4.1.1	Root-locus technique.....	27
4.1.2	Proportional-Integral-Derivative technique .....	31
4.1.3	PID Tuning.....	32
4.1.4	Controlled System Response Analysis.....	34
4.2	Closed Loop Controller Application.....	36
4.2.1	Summer Evaluation.....	36
4.2.2	Winter Evaluation .....	37
4.2.3	Further System Evaluation .....	37
4.3	Controller Performance Discussion .....	38
4.3.1	Notable Results .....	38
4.3.2	Model Limitations .....	42
4.4	Necessary Instrumentation.....	43
5	Conclusion.....	45
6	References .....	46
7	Appendices .....	a
7.1	Appendix A – Relevant Code Used .....	a

## LIST OF FIGURES

Figure 1: Solar radiation density in South Africa [9].	2
Figure 2: Layout of old-age home.	3
Figure 3: Type of currently implemented solar tracking.	5
Figure 4: Azimuth axis angle throughout the 21 <sup>st</sup> day of every month for a year.	6
Figure 5: Azimuth axis angle throughout the Summer and Winter Solstices.	6
Figure 6: Azimuth axis path for both Summer and Winter Solstices.	7
Figure 7: Azimuth axis rotation for the chosen configuration of solar panel.	8
Figure 8: Schematic representation of the solar panel-motor system.	9
Figure 9: Diagram showing the projected area of the solar panel to the wind.	10
Figure 10: Simulink diagrammatic representation of the solar panel-motor system.	12
Figure 11: Simulink representation of the motor.	12
Figure 12: Simulink representation of the solar panel.	12
Figure 13: Physical properties relating to the chosen solar panel.	15
Figure 14: Unity feedback closed-loop transfer function.	16
Figure 15: Linear System Nyquist Plot.	18
Figure 16: General form of the Nyquist Plot in the s-plane.	18
Figure 17: Analytically derived Nyquist Plot.	21
Figure 18: Linear System Bode Plot.	22
Figure 19: Non-linear system responses to various excitations.	23
Figure 20: Comparison of Linear and Non-Linear System Step Input Response.	24
Figure 21: Diagrammatic representation of the general Root Locus behaviour.	30
Figure 22: Controlled system's response to various input functions.	34
Figure 23: Comparison of solar tracking performance between the controlled and uncontrolled system for the summer solstice.	36
Figure 24: Comparison of solar tracking performance between the controlled and uncontrolled system for the winter solstice.	37
Figure 25: System response to a random disturbance.	38
Figure 26: Daily required motor voltage input.	39
Figure 27: Change in irradiation over time for summer and winter solstices.	40
Figure 28: Solar panel power generation over summer and winter solstices.	41
Figure 29: Cumulative power capacity of the solar panel for summer and winter solstices.	41
Figure 30: Solar Panel Spacing Distribution.	42

## LIST OF TABLES

Table 1: Power consumption for a single housing unit.....	3
Table 2: Energy generation requirements. ....	4
Table 3: Descriptions of currently implemented solar tracking.....	5
Table 4: DB-4000 Matrix Motor Specifications [19] .....	15
Table 5: Relevant input parameters for the Model Lineariser App.....	16
Table 6: Routh-Hurwitz stability analysis .....	17
Table 7: Points of interest for Case A. ....	20
Table 8: Points of interest for Case B. ....	20
Table 9: Comparison of performance parameters for linear and non-linear systems .....	25
Table 10: Routh-Hurwitz stability analysis .....	31
Table 11: Common drawbacks of over/under tuned systems. ....	32
Table 12: Parameters of the Control Design Toolbox tuner .....	33
Table 13: Final system specifications. ....	45

## NOMENCLATURE

$T_{wind}$	- Torque caused by the wind
$r$	- Half the width of the chosen solar panel
$\rho$	- Air Density
$C_D$	- Drag coefficient of the chosen solar panel
$U_\infty$	- Freestream wind velocity
$\omega$	- Rotational velocity of the chosen solar panel
$\alpha$	- Set orientation of the chosen solar panel
$L$	- Length of the chosen solar panel
$J_{eq}$	- Equivalent moment of inertia on the solar panel side of the gearing system
$\theta$	- Angle of the chosen solar panel
$\frac{d\theta}{dt} \equiv \dot{\theta}$	- Angular velocity of the chosen solar panel
$\frac{d^2\theta}{dt^2} \equiv \ddot{\theta}$	- Angular acceleration of the chosen solar panel
$K_{d,eq}$	- Equivalent damping coefficient of the motor on the solar panel side of the gearing system
$K_s$	- Spring constant
$L_a$	- Armature inductance
$i_a$	- Armature current
$\frac{di_a}{dt}$	- Armature current rate of change
$V$	- Input voltage
$K_e$	- Back emf constant
$R_a$	- Armature DC resistance
$T_{motor,eq}$	- Developed motor torque on the solar panel side of the gearing system
$K_{t,eq}$	- Motor torque constant on the solar panel side of the gearing system
$F$	- Function
$F_L$	- Linearised function
$F_0$	- Function evaluated at operating conditions
$\left(\frac{\delta F}{\delta \theta}\right)_0$	- Partial derivative of function with respect to angular position, evaluated at operating conditions
$\Delta\theta$	- Perturbation of angular position
$\left(\frac{\delta F}{\delta \dot{\theta}}\right)_0$	- Partial derivative of function with respect to angular velocity, evaluated at operating conditions



$\Delta\dot{\theta}$	- Perturbation of angular velocity
$\left(\frac{\delta F}{\delta\ddot{\theta}}\right)_0$	- Partial derivative of function with respect to angular acceleration, evaluated at operating conditions
$\Delta\ddot{\theta}$	- Perturbation of angular acceleration
$\left(\frac{\delta F}{\delta T_{motor}}\right)_0$	- Partial derivative of function with respect to motor torque, evaluated at operating conditions
$\Delta T_{motor}$	- Perturbation of motor torque
$\frac{\theta(s)}{V(s)}$	- System transfer function
$W$	- Width of the chosen solar panel
$H$	- Height of the chosen solar panel
$m$	- Mass of the chosen solar panel
$T_p$	- Peak torque of the chosen motor
$K_d$	- Viscous damping coefficient of the chosen motor
$J_M$	- Rotor inertia of the chosen motor
$m_{motor}$	- Mass of the chosen motor
$K_t$	- Motor torque constant of the chosen motor
$V_{max}$	- Maximum voltage of the chosen motor
$P(s)$	- Equivalent system transfer function
$N(s)$	- Numerator of system transfer function
$D(s)$	- Denominator of system transfer function
$Z$	- Number of zeroes
$P$	- Number of poles
$\theta_k$	- Asymptote
$\sigma$	- Asymptote centroid
$\Sigma s_p$	- Sum of poles
$\Sigma s_z$	- Sum of zeroes
$K$	- Gain margin
$\frac{dK}{ds}$	- Breakaway condition
$K_p$	- Proportional gain
$K_I$	- Integral gain
$K_D$	- Derivative gain
$e(t)$	- Error signal

$N$	- Filter coefficient
$P_{avg}$	- Average power
$V_{avg}$	- Average voltage
$n$	- Number of solar panels required

# 1 INTRODUCTION

Solar power has emerged as a highly popular alternative energy source in response to the ongoing load shedding issues faced in South Africa [1]. In modern life, consistent access to electricity has become indispensable, with most aspects of daily living relying on it. Consequently, experiencing load shedding often disrupts tasks and routines, leading to a reduction in overall quality of living and productivity [2]. Despite plans to increase energy supply capabilities in South Africa, building and developing the necessary infrastructure takes time. This delay means the current electricity dilemma cannot be quickly resolved. Consequently, individuals and communities must rely on alternative solutions to manage the shortage, which places a significant financial strain on them.

While other solutions, such as using a generator, exist to combat load shedding, there are numerous benefits to opting for solar power. High quality generators are capital intensive and have high operating costs, particularly due to increasing fuel costs and large maintenance requirements [3]. Additionally, generators are significant sources of noise and chemical pollution, making them an unsustainable solution [4]. Although solar systems are heavily capital intensive [5], their long-term running costs and sustainability are far superior to those of generators. The prices of solar panels and installation are rapidly decreasing, making them increasingly accessible [6]. Additionally, government incentives and financing options are available to help offset initial costs. As a result, the adoption of solar energy is expected to increase significantly in the coming years.

A notable limitation of solar energy is its space requirements. In some cases, limited space can prevent the solar system from meeting performance specifications, prolonging the payback period. Consequently, users may still experience load shedding due to insufficient energy generation. Generating a significant amount of electricity from solar energy typically requires a large area with unobstructed sunlight. This can be challenging for properties that have limited roof space or are shaded by trees, neighbouring buildings, or other obstructions [5]. One solution to this issue involves improving the effectiveness of the solar power system by ensuring that the angle between the sun and the solar panel is always optimal. This can be achieved by using a solar tracker that adjust the panel to remain perpendicular to the sun's rays. However, solar trackers require an intensive control system and additional components, which can increase startup and maintenance costs. Therefore, solar trackers are typically only used in scenarios with spacing restrictions, while stationary solar farms remain more economically viable when sufficient space is available to meet power requirements.

The renewable energy sector is experiencing a surge in demand for the development of solar tracking systems [7], where developments are focused on improving system performance, and lowering system start-up costs. As these factors improve with time, solar tracker systems will be increasingly adopted by both large-scale solar farms and home-based solar setups [8]. This increase in the efficiency of solar farms would prove to be highly beneficial to the renewable energy sector, and to society.

## 1.1 Environmental Factors

The efficacy of a solar panel system hinges on environmental factors, including a location's inherent weather conditions (whether it is often sunny or cloudy) and the availability of sufficient solar irradiation. Consequently, while the load shedding crisis is prevalent nationwide, solar power proves more effective in some areas than others. Figure 1 illustrates the distribution of solar radiation across the country. It reveals that the North-Western regions experience high levels of solar radiation, making solar energy solutions highly applicable, whereas the Southern and Eastern regions receive less solar radiation annually. This doesn't negate the viability of solar energy in these areas but underscores the need to explore alternative renewable energy sources, such as wind power, with increasing consideration.

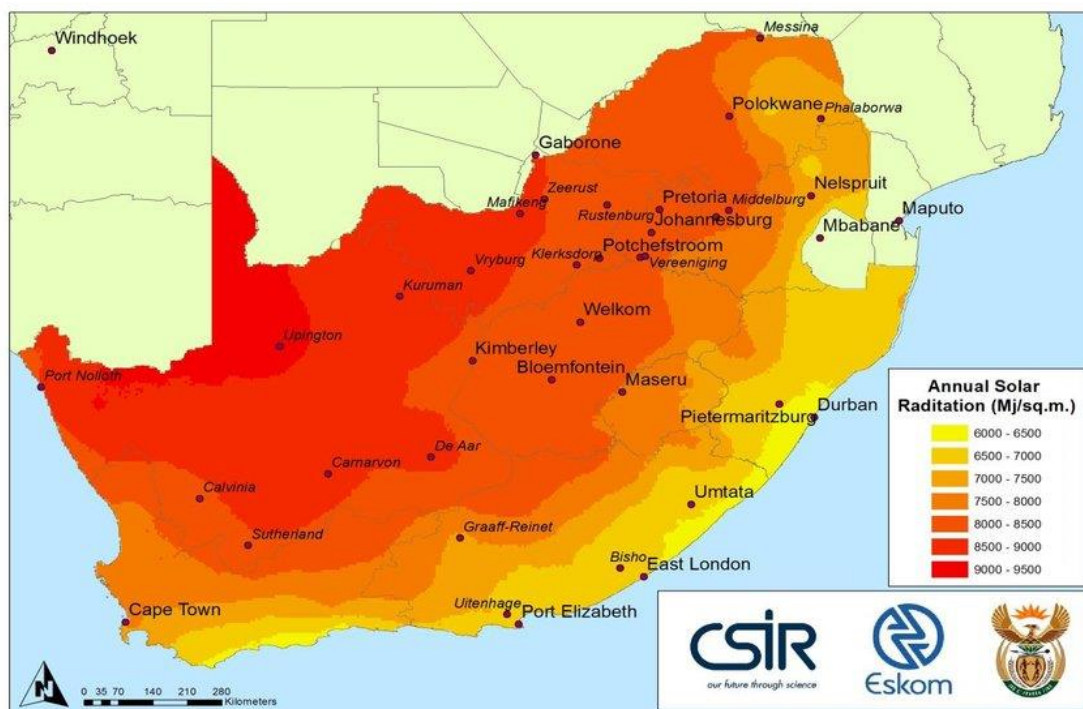


Figure 1: Solar radiation density in South Africa [9].

## 1.2 Scenario Development

For this report, the scenario is as follows:

A small-scale old age home in Upington, South Africa, is under large financial strain to meet the electricity demands of its residents, who require a stable electricity supply for healthcare assistance devices, daily tasks, and entertainment [10]. Due to the city's commitment to expanding solar energy generation, as evidenced by the presence of large solar parks within the city [11], smaller-scale businesses are encouraged to invest in solar power systems. Consequently, considering this initiative and the city's high annual solar radiation (as shown in Figure 1), the old age home has concluded that implementing a small solar farm as a back-up power supply is feasible to meet their power needs. The

home experiences a maximum of 6 hours of load shedding per day, and so the back-up system should be able to generate a minimum of 25% of their daily usage requirements within a day. Additionally, the old age home will have a power storage system capable of supplying the home with power during times where power generation is unstable.

Whilst the home has two plots of 20 x 50 m of available land, as displayed in Figure 2, the residents have requested that one plot remains untouched. Because of this request and the power requirements of the home, a fixed-tilt solar farm is deemed inadequate. The purpose of this report is to develop a solar tracker system suitable for the old-age home and determine whether the power supply from the solar farm with solar trackers would be sufficient for the home.

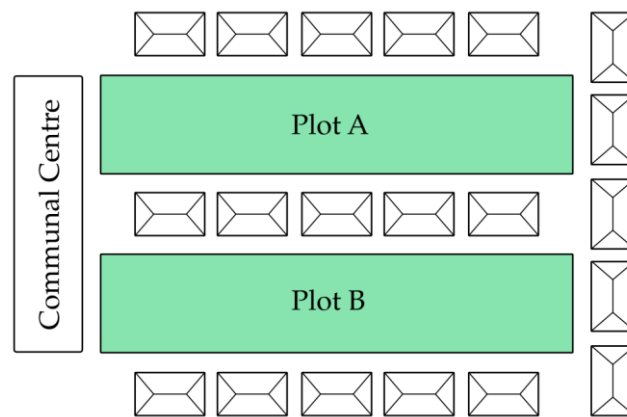


Figure 2: Layout of old-age home.

Prior to the development of the system, it is necessary to develop the system requirements. These are to form success criteria, for which the completed solar tracker will be evaluated against. To determine the necessary power requirements, the old-age home has provided the typical power usage statistics per house, per day, in Table 1. The home has indicated that they have five residents using healthcare assistance devices of 45 W for 24 hours a day.

Table 1: Power consumption for a single housing unit.

Appliance	Time [hr/day]	Power Consumption [kWh]	Appliance	Time [hr/day]	Power Consumption [kWh]
<b>Kitchen</b>			<b>Living Room</b>		
Fridge	24	1.416	TV	5	1
Freezer	24	1.248	Fan	5	0.6
Oven	1	1.2	Lights	5	0.36
			<b>Bedroom</b>		
Stove	0.5	0.6	Fan	8	0.96
Microwave	0.17	0.167	Lights	3	0.072
Dishwasher	0.5	0.65			

Kettle	0.17	0.2	<b>Bathroom</b>		
Toaster	0.083	0.071	Lights	1	0.072
Lights	2	0.144			

Appliance	Time [hr/day]	Power Consumption [kWh]
<b>Extra Appliances</b>		
Wi-Fi Router	24	0.168
Vacuum Cleaner	0.286	0.286
PC	1	0.3
Clothes Iron	0.286	0.343
Washing Machine	0.143	0.114
Tumble Dryer	0.143	0.429
Geyser	1	4.5
<b>Total</b>	-	14.935

This approximation is then used to estimate the total power requirements of the system, by considering the number of units in the home, and the additional healthcare power requirements. The total power the system is required to generate, per day, is depicted in Table 2:

Table 2: Energy generation requirements.

	Number of units	Electricity per unit per day (kWh)	Total Electricity per day (kWh)
<b>Housing</b>	20	14.935	298.7
<b>Healthcare</b>	5	1.08	5.4
<b>Total</b>		0.25(298.7 + 5.4)	<b>76.025 kWh</b>

### 1.3 Problem Summary

Maintaining the optimal incidence angle between solar panels and the sun is crucial for maximizing energy capture. Fixed solar panels often fail to achieve this, leading to suboptimal performance. To address this, a solar panel axis control system will be designed to ensure the panels consistently achieve the optimal angle with respect to sunlight. This system will utilize a simulation-based control mechanism to allow rotational movement about one axis, maximizing energy absorption and efficiency. The overall aim is for the solar panels to accurately follow the sun's path, ensuring they are always in the best position to capture sunlight.

## 2 SYSTEM DESIGN AND MODELLING

### 2.1 Sun Positioning and Types of Solar Tracking

When implementing solar tracking, there are two main axes to consider: azimuth and elevation, as can be seen in Figure 3, subsequently being compared in Table 3:

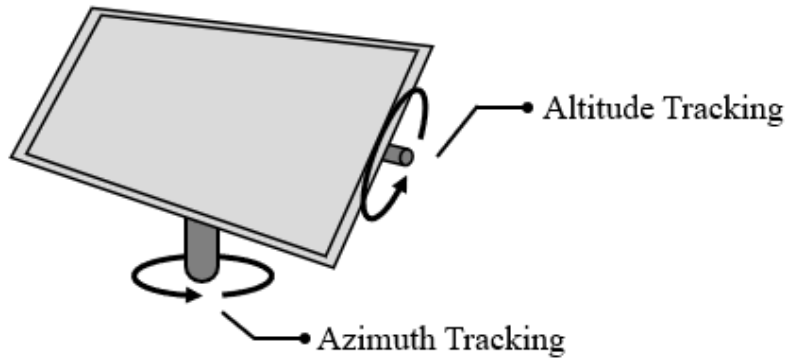


Figure 3: Type of currently implemented solar tracking.

Table 3: Descriptions of currently implemented solar tracking.

Tracking Type	Description
<b>Azimuth</b>	Adjusts the orientation of the solar panel horizontally to match the apparent motion of the sun.
<b>Elevation</b>	Adjusts the tilt of the solar panel vertically to track the altitude motion of the sun.

With the primary focus of the development of the solar tracker within this report focusing on maximising energy production, azimuth tracking was chosen for solar panel implementation. The reason being that azimuth tracking, achieved by adjusting the panels' horizontal orientation, ensures direct sun exposure throughout the day, thereby optimising solar radiation capture. Consequently, this enhances energy production while further fostering a more consistent energy output [12].

It is important to acknowledge that the azimuth angle exhibits significant variability throughout the year, particularly noticeable in the southern hemisphere. For example, approaching the winter solstice in June, the azimuth range tends to be shorter compared to the months leading up to the summer solstice in December, as depicted in Figure 4, with ( $t=0$ ) indicating sunrise. These graphical representations were produced using MATLAB code, outlined in detail in Appendix A, which processed azimuth angles derived from sunrise and sunset data for the specific date in question. Subsequently, azimuth angle plots

for the 21st of each month, spanning from January to December, were generated and are provided in Figure 4 below.

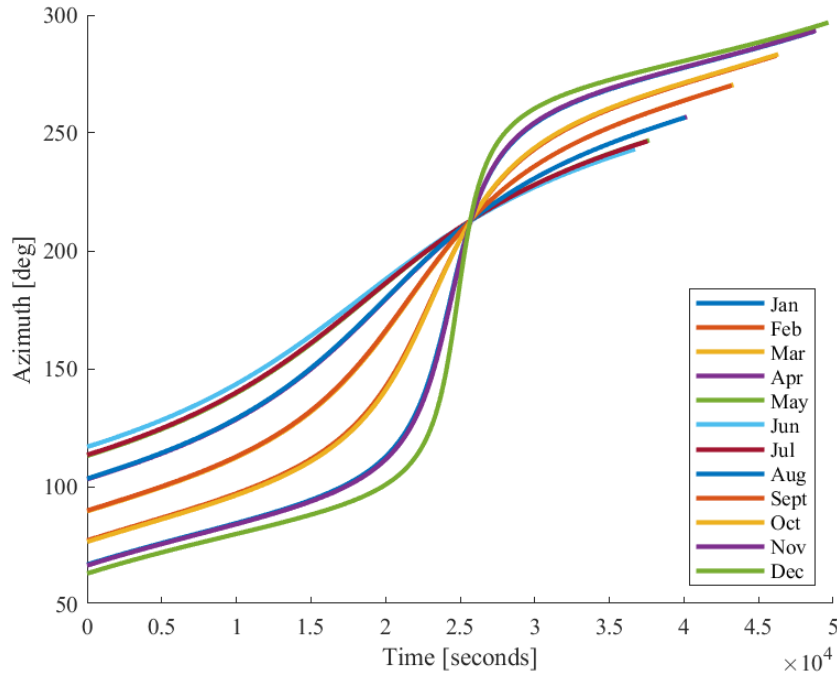


Figure 4: Azimuth axis angle throughout the 21<sup>st</sup> day of every month for a year.

Following this observation, two significant design focal points emerged: the winter and summer solstices, which respectively occur in June and December. Notably, the 21st of these months precisely corresponds to the solstice occurrences, as illustrated in Figure 5, where (t=0) denotes sunrise.

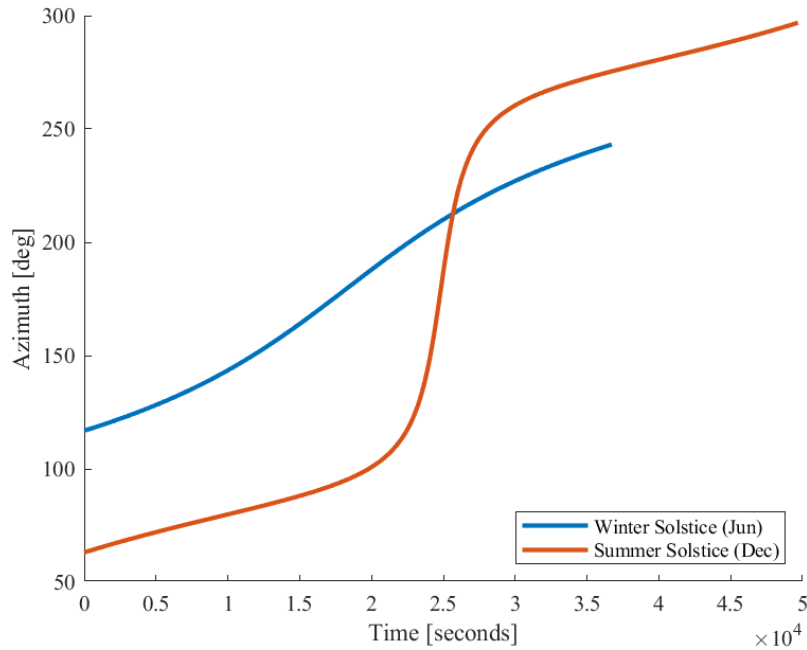


Figure 5: Azimuth axis angle throughout the Summer and Winter Solstices.



Subsequently, the performance of the resulting control system is benchmarked against the sun information of these two days, corresponding to the shortest and longest daylight hours respectively.

With this in mind, the azimuth angle can be further defined as the angle of the sun's rays measured in the horizontal plane due north (for the southern hemisphere), where South is represented by  $\theta = 0^\circ$ , as shown in Figure 6:

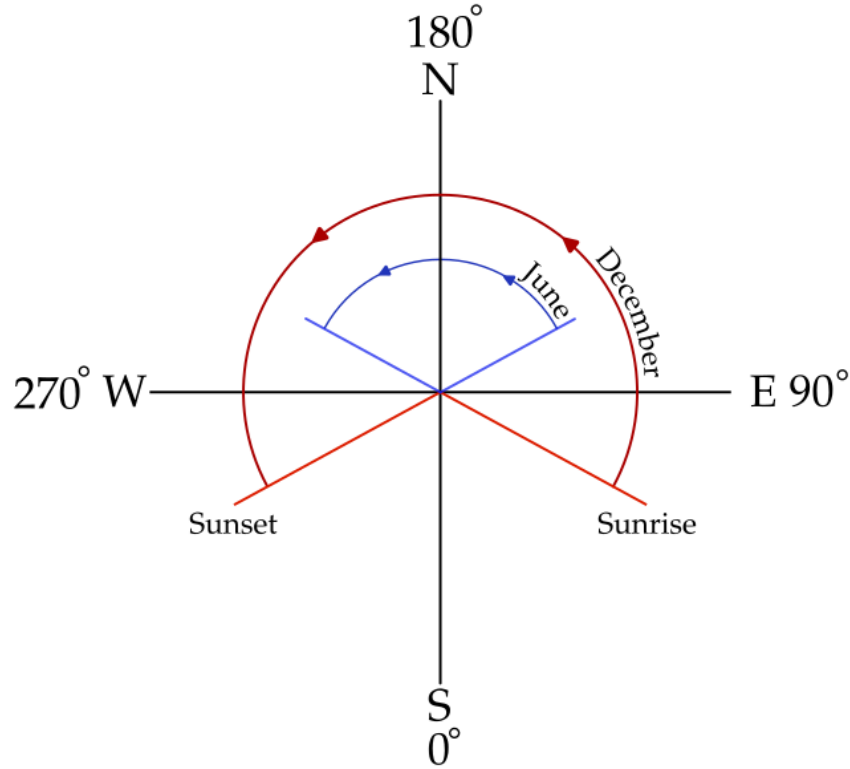


Figure 6: Azimuth axis path for both Summer and Winter Solstices.

Thus, it can be seen that for the winter solstice, the sun rises in the northeast quadrant, and sets in the northwest quadrant, whilst for the summer solstice, the sun rises in the southeast quadrant, and sets in the southwest quadrant.

## 2.2 Non-linear Model Development

### 2.2.1 Design Decisions

With the power requirements clearly outlined, it is necessary to make decisions regarding the system design. As such, the purpose of this section is to briefly describe each design decision made throughout the process as well as the rationale behind it. Subsequently, these decisions form the backbone of the model formulation to come.

Decision 1: Motor controlled rotation – Directly controlling the rotation of the panels via a motor minimises the quantity of components required and eliminates the design complexity introduced with mechanical linkages.

Decision 2: Solar panel orientation – The solar panel's orientation was chosen to be such that the width dimension of the panel is facing towards the floor, as shown in Figure 7. This reduces the moment of inertia about the vertical axis, thus minimising motor torque and power requirements.

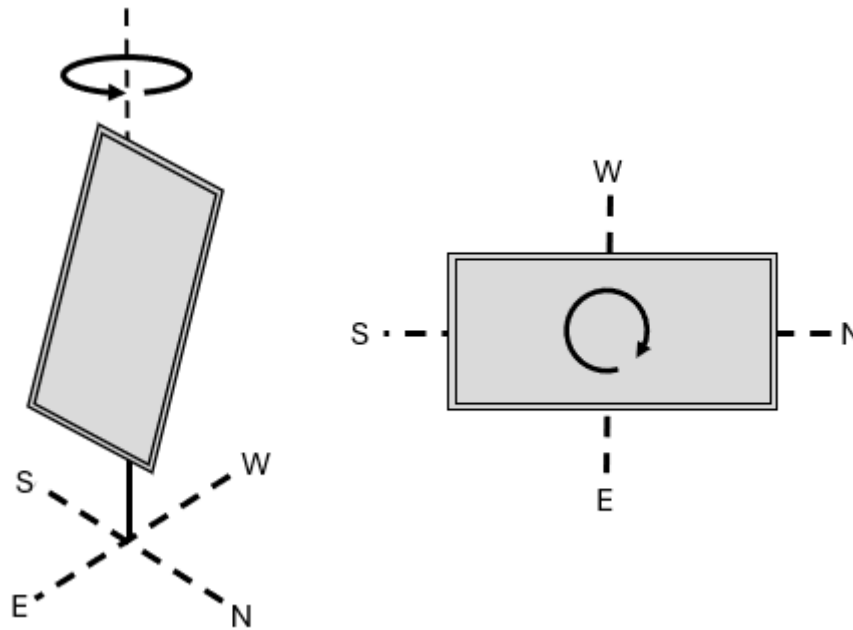


Figure 7: Azimuth axis rotation for the chosen configuration of solar panel.

Decision 3: Solar panel orientation – The solar panel's orientation is chosen to be  $30^\circ$  from the horizontal plane. This angle is commonly used for azimuth based solar trackers [13]

Decision 4: Armature-Controlled DC Motor – The control motor was chosen to be modelled as an Armature-Controlled DC motor. Such motors are commonly used where precise speed control is required, which is beneficial in a control scenario.

Decision 5: Gearing Ratios – The motor output is applied through a series of gears with a gear ratio of 1:2.

Decision 6: Position reset - A torsional spring is used to smoothly return the panel to its desired position for the following day, with a spring rate chosen relative to the motor's stall torque. As the sun sets, the motor torque gradually decreases until it reaches a calculated value, at which point the torque of the spring matches that of the motor, aligning the panel at the necessary angle for the next day, and locking the motor.

### 2.2.2 Assumptions

The development of the non-linear model requires certain assumptions. These assumptions serve one of two purposes:

1. To simplify mathematical complexity, or
2. To approximate complex phenomena, such as wind, which are not perfectly constant or predictable.

The relevant assumptions are as follows:

- The average wind direction in Uppington was taken to be from West to East, when modelling the wind torque [14].
- The average wind speed in Uppington was taken to be 7 knots (3.6 m/s), when modelling the wind torque [14].
- The average density in Uppington was taken to be  $1.09 \text{ kg/m}^3$  [15]
- The latitude of Uppington was taken to be  $-28.4508^\circ$  [16]
- The solar panel is assumed to be a flat plate, with a constant drag coefficient ( $C_D$ ) of 1.17 [17]

### 2.2.3 Model Formulation

The envisioned model comprises of a motor, a geared system, and a solar panel. In this setup, the motor is connected to the solar panel via a step-down gear ratio, as depicted in Figure 8.

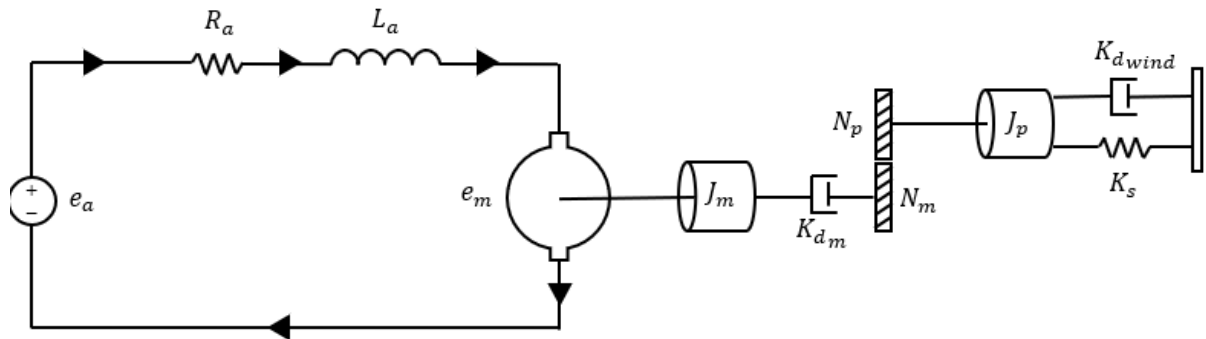


Figure 8: Schematic representation of the solar panel-motor system.

As such, to develop a complete mathematical model for the physical system, the following relationships need to be derived:

1. A relationship between the torque induced by the wind and solar panel's current angle of rotation.
2. The equation of motion of the solar panel, relating the sum of torques to rotational acceleration.
3. The governing equation of the motor, relating the input voltage to the circuit current.
4. A relationship between the circuit current and motor torque.

### 2.2.3.1 Wind-induced-torque

Although the absolute wind speed on either side of the panel equalizes, the relative air speed, influenced by the panel's rotation (with one side moving into the wind and the other moving away), generates a torque around the rotational axis. To establish a relationship for this wind-induced torque, the maximum torque—occurring when the panel directly faces the wind—was calculated and then adjusted by a factor of  $\sin(\theta)$ . This factor represents the changing projected area of the panel as it rotates.

The relationship for the maximum torque generated was determined using equation 2.1,

$$T_{wind} = \int_{-r}^r \frac{1}{2} r \rho L C_D (U_{\infty} + \omega r)^2 \sin(\alpha) dr \quad (2.1)$$

where  $r$  is half the width of the panel,  $\rho$  is the air density,  $L$  is the length of the panel,  $C_D$  is the drag coefficient,  $U_{\infty}$  is the freestream velocity of the wind,  $\omega$  is the rotational velocity of the panel, and  $\alpha$  is the set orientation of the panel, as represented in Figure 9.

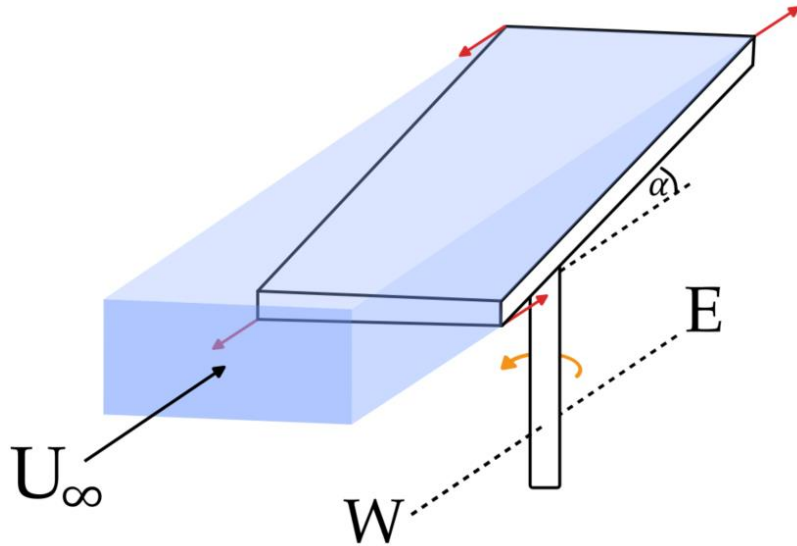


Figure 9: Diagram showing the projected area of the solar panel to the wind.

This relationship reduces to a wind torque coefficient multiplied by the current speed and orientation of the panel, as shown in equations 2.2 through 2.4:

$$= \frac{1}{2} \rho L C_D \sin(\alpha) \int_{-r}^r r U_{\infty}^2 + 2\omega r^2 U_{\infty} + \omega^2 r^3 dr \quad (2.2)$$

$$= \frac{1}{2} \rho L C_D \sin(\alpha) \left[ \frac{r^2}{2} U_{\infty}^2 + \frac{2}{3} \omega r^3 U_{\infty} + \frac{\omega^2 r^4}{4} \right]_{-r}^r \quad (2.3)$$

$$T_{wind} = \left[ \frac{2}{3} \rho L C_D \sin(\alpha) [r^3 U_{\infty}] \right] |\sin(\theta) \omega| \text{ (Against direction of rotation)} \quad (2.4)$$

### 2.2.3.2 Solar panel equation of motion

The equation of motion for the solar panel is found using the rotational form of Newton's second law. This is used to relate the solar panel's acceleration to the sum of torques acting around the vertical axis, as seen in equations 2.5 and 2.6,

$$J_{eq} \frac{d^2\theta}{dt^2} = T_{motor,eq} - T_{wind} - T_{damping,eq} - T_{spring} \quad (2.5)$$

$$J_{eq} \frac{d^2\theta}{dt^2} = T_{motor,eq} - \frac{d\theta}{dt} \left[ \left| \frac{2}{3} \rho L C_D (r^3 U_\infty \sin(\theta)) \right| + K_{d,eq} \right] - \theta K_s \quad (2.6)$$

where  $J$  represents moment of inertia,  $\theta$  represents the angle of the panel,  $K_d$  represents the damping coefficient of the motor,  $K_s$  represents the spring constant, and the subscript  $eq$  indicates that the variable is the equivalent variable on the solar panel side of the gear system.

### 2.2.3.3 Motor governing equation

The governing equation for the motor is found using Kirchhoff's Voltage Law. This is used to relate the input voltage to the sum of voltage drops around the loop, and hence, the current in the armature system, as seen in equation 2.7,

$$L_a \frac{di_a}{dt} = V - K_{e,eq} \frac{d\theta}{dt} - R_a i_a \quad (2.7)$$

where  $L_a$  is the armature inductance,  $i_a$  is the armature current,  $V$  is the input voltage,  $K_e$  is the back EMF constant,  $R_a$  is the DC resistance of the armature, and once again, the subscript  $eq$  indicates that the variable is the equivalent variable on the solar panel side of the gear system.

### 2.2.3.4 Relationship between circuit current and motor torque

For an armature-controlled DC motor, the developed torque is directly proportional to the armature current. As such, the relationship is as seen in equation 2.8,

$$T_{motor,eq} = K_{t,eq} i_a \quad (2.8)$$

where  $K_t$  is the motor torque constant, and the subscript  $eq$  represents the equivalent variable on the panel side of the gear system.

## 2.2.4 Simulink Representation

A Simulink model of the non-linear mathematical system is necessary for further analysis, as the analytical techniques used in this report are only suitable for linear models. An overview of the developed unity feedback Simulink model is provided in Figure 10, with the motor and panel models detailed in Figures 11 and 12 respectively. The wind disturbance model is represented by inputting equation 4 as a MATLAB function.

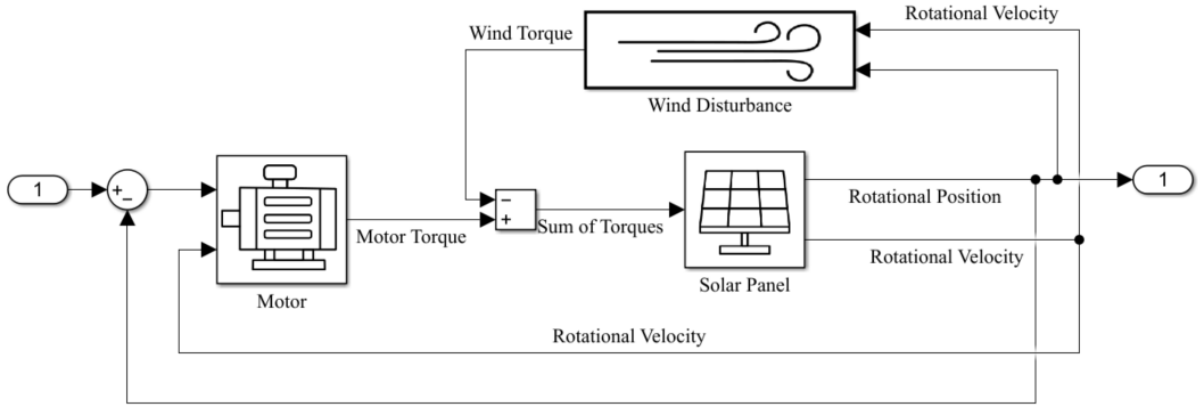


Figure 10: Simulink diagrammatic representation of the solar panel-motor system.

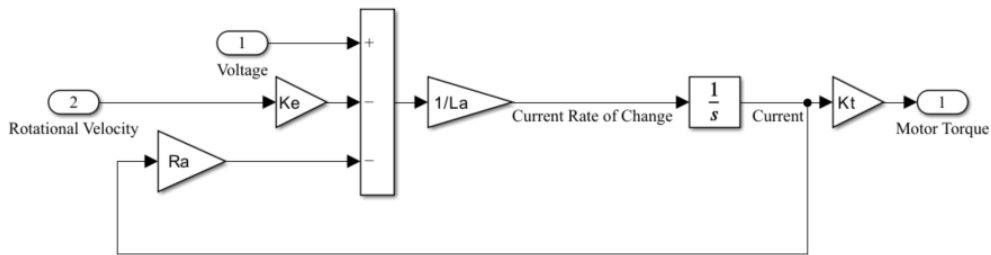


Figure 11: Simulink representation of the motor.

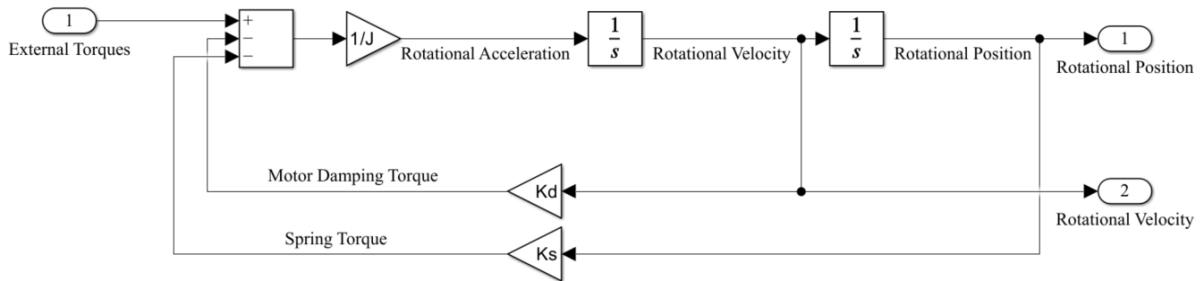


Figure 12: Simulink representation of the solar panel.

## 2.3 Model Linearisation

The presence of the nonlinear  $\sin(\theta)$  term in equation 6 necessitates linearizing the equation to develop a transfer function and apply linear analytical techniques. The linearization approach used involves applying the Taylor Series expansion about a suitable equilibrium point.

### 2.3.1 Operating point

For the purpose of this report, the equation is chosen to be linearized about the sunrise position on the summer solstice. This decision is dual-purposed:

1. The summer solstice is chosen because it represents the days with the longest sunlight cycle, requiring the control system to be consistent over the largest period of time, and it is when the spring generates an increasingly large torque on the system that the motor must act against.
2. The sunrise position is chosen because it is the only time of day that satisfies the equilibrium conditions of  $\dot{\theta} = 0$  and  $\ddot{\theta} = 0$ . At this point, as outlined in Section 2.1.1, the angular position of the panel is  $\theta = 63.134^\circ$ , and the motor torque equals the spring torque.

### 2.3.2 Linearisation

The linearisation process using the Taylor Series expansion, with the equilibrium points as described in Section 2.3.1, begins with denoting the function,  $F$ , as follows:

$$F = J_{eq}\ddot{\theta} + C_1\dot{\theta} + K_s\theta - T_{motor} = 0 \quad (2.9)$$

where

$$C_1 = \frac{2}{3}\rho r^3 C_D L U_\infty \sin(30) |\sin(\theta)| + K_{d,eq} \quad (2.10)$$

Following this, the linearised function,  $F_L$  is as described in equations 2.11 to 2.13:

$$F_L = F_0 + \left(\frac{\delta F}{\delta \theta}\right)_0 \Delta\theta + \left(\frac{\delta F}{\delta \dot{\theta}}\right)_0 \Delta\dot{\theta} + \left(\frac{\delta F}{\delta \ddot{\theta}}\right)_0 \Delta\ddot{\theta} + \left(\frac{\delta F}{\delta T_{motor}}\right)_0 \Delta T_{motor} = 0 \quad (2.11)$$

where

$$\Delta\theta = \theta - \theta_0; \Delta\dot{\theta} = \dot{\theta} - \dot{\theta}_0; \Delta\ddot{\theta} = \ddot{\theta} - \ddot{\theta}_0; \Delta T_{motor} = T_{motor} - T_{motor,0} \quad (2.12)$$

and

$$F_0 = F(\theta_0, \dot{\theta}_0, \ddot{\theta}_0, T_0) = 0 \quad (2.13)$$

The results of the partial differentiations are as follows:

$$\left(\frac{\delta F}{\delta \theta}\right)_0 \Delta\theta = \left(\frac{2}{3}\rho r^3 C_D L U_\infty \sin(30) |\cos(\theta)|\dot{\theta} + K_s\right)_0 \Delta\theta = K_s \Delta\theta \quad (2.14)$$

$$\left(\frac{\delta F}{\delta \dot{\theta}}\right)_0 \Delta\dot{\theta} = \left(\frac{2}{3}\rho r^3 C_D L U_\infty \sin(30) |\sin(\theta)| + K_d\right)_0 \Delta\dot{\theta} \quad (2.15)$$

$$\left(\frac{\delta F}{\delta \ddot{\theta}}\right)_0 \Delta\ddot{\theta} = (J_{eq})_0 \Delta\ddot{\theta} = J_{eq} \Delta\ddot{\theta} \quad (2.16)$$

$$\left(\frac{\delta F}{\delta T_{motor}}\right)_0 \Delta T_{motor} = (-1)_0 \Delta T_{motor} \quad (2.17)$$

This gives a final, linearised equation of motion for the solar panel:

$$F_L = J_{eq}\Delta\ddot{\theta} + C\Delta\dot{\theta} + K_s\Delta\theta - \Delta T_{motor} \quad (2.18)$$

where

$$C = \frac{2}{3}\rho r^3 C_D L U_\infty \sin(30) |\sin(\theta_0)| + K_d \quad (2.19)$$

### 2.3.3 Transfer Function

Having linearised the three primary system equations, it is possible to determine a transfer function. As such, the desired transfer function is of the form:

$$\text{Transfer Function} = \frac{\text{Output}}{\text{Input}} \quad (2.20)$$

where the output is the rotational position,  $\theta(s)$ , and the input is the voltage input of the motor,  $V(s)$ . This function is derived by taking the Laplace transform of both the linearised solar panel's equation of motion and the motor's governing equation, and then coupling them with the Laplace transform of the relationship between the armature current and motor torque, as described in Equation 2.8. The Laplace transforms of the linearised solar panel equation of motion and the motors governing equation can be seen in equation 2.20 and 2.21 respectively.

$$J_{eq}s^2\theta(s) + Cs\theta(s) + K_s\theta = T(s) \quad (2.21)$$

$$L_a sI(s) + K_{e,eq}s\theta(s) + RI(s) = V(s) \quad (2.22)$$

These transfer functions are coupled by the following relationship:

$$I(s) = \frac{T(s)}{K_{t,eq}} \quad (2.23)$$

Which simplifies to the following transfer function, representative of the linearised control plant:

$$\frac{\theta(s)}{V(s)} = \frac{\frac{K_{t,eq}}{J_{eq}L_a}}{s^3 + \left(\frac{R_a}{L_a} + \frac{C}{J_{eq}}\right)s^2 + \left(\frac{R_a C + K_{e,eq}K_{t,eq}}{J_{eq}L_a} + \frac{K_s}{J_{eq}}\right)s + \frac{RK_s}{J_{eq}L_a}} \quad (2.24)$$

### 2.3.4 System Specifications

The solar panel is modelled after the Sankopower 550W Monocrystalline Solar Panel, which has the following important dimensions, indicated by Figure 13 [18]:



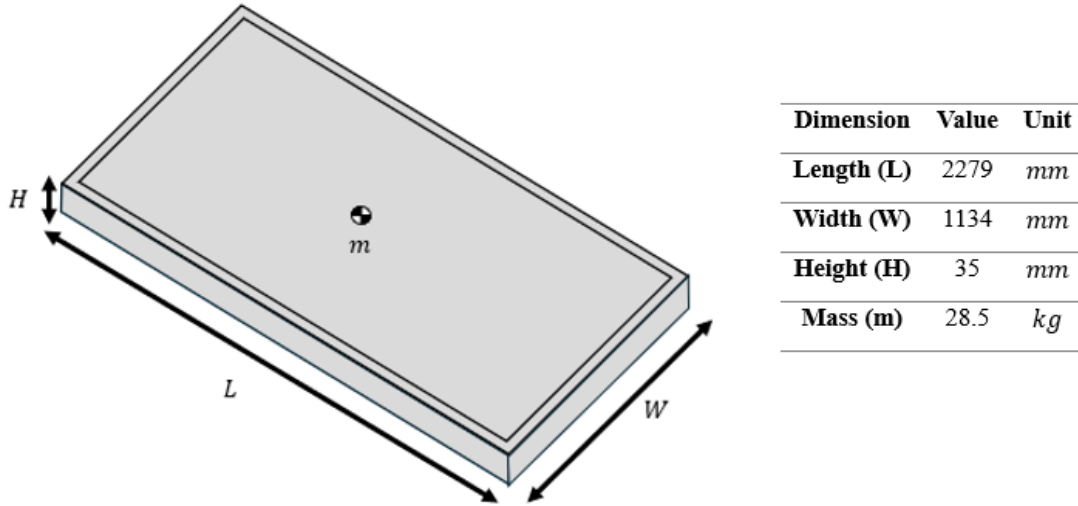


Figure 13: Physical properties relating to the chosen solar panel.

The armature-controlled DC motor is modelled after the Moog DB-4000 Matrix DC Motor, with important specifications as seen in Table 4 [19]:

Table 4: DB-4000 Matrix Motor Specifications [19]

Variable	Value	Equivalent Value After Gear System	Unit
Peak Torque [ $T_p$ ]	14.123	28.246	Nm
Viscous Damping Coefficient [ $K_d$ ]	1.464	2.928	Nms/rad
Rotor Inertia [ $J_M$ ]	0.0071	0.0284	kg.m <sup>2</sup>
Mass [ $m_{motor}$ ]	21.769	21.769	kg
Motor Torque Constant [ $K_t$ ]	0.4695	0.939	Nm/A
Back EMF Constant [ $K_e$ ]	0.469	0.938	Vs/rad
Armature Inductance [ $L_a$ ]	3.2	3.2	mH
Armature Resistance [ $R_a$ ]	0.98	0.98	$\Omega$
Maximum Voltage [ $V_{max}$ ]	27.5	—	V

Using the above equivalent system parameters, the open-loop transfer function is as seen in equation 2.24:

$$\frac{\theta(s)}{V(s)} = \frac{23.7894}{s^3 + 306.7708s^2 + 182.0498s + 71.4275} \quad (2.25)$$

### 2.3.5 Linearisation Validation

The Model Lineariser App in Simulink provides tools to facilitate the linearisation of a non-linear Simulink Models. This process considers relevant linear analysis points, such as open loop inputs, open loop outputs, and operating conditions – all of which being defined by the user according to their needs. As such, in an effort to validate the linearised model of the physical system obtained through hand calculations, Table 5 was defined:

Table 5: Relevant input parameters for the Model Lineariser App

Required Information	Provided Value
Analysis I/O Input	Voltage supplied to the motor ( $V$ )
Analysis I/O Output	Position of the solar panel ( $\theta$ )
Operating Point	As defined in Section 2.3.1

With the necessary linearisation I/Os defined, and the appropriate operating conditions set, the model was linearised using a step input function, yielding the following open loop transfer function:

$$\frac{\theta(s)}{V(s)} = \frac{23.79}{s^3 + 306.77s^2 + 182.05s + 71.43} \quad (2.26)$$

Thus, it can be seen that the transfer functions obtained from both the hand calculations, and the MATLAB Model Lineariser App are in close agreement, thereby confirming the accuracy and validity of the final proposed transfer function.

### 2.3.6 Linear Simulink Model

Subsequently, Simulink is to be utilised as part of linearised model analysis, with the validate transfer function as defined in Section 2.3.5. Thus, the unity-feedback closed-loop transfer function is represented in Simulink using the ‘Transfer Function with Initial Outputs’ block, as shown in Figure 14:

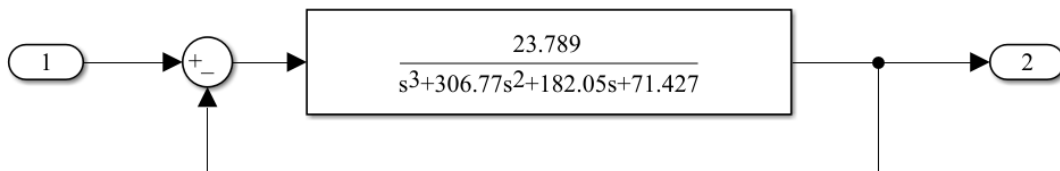


Figure 14: Unity feedback closed-loop transfer function.

### 3 SYSTEM ANALYSIS

#### 3.1 Stability Analysis

##### 3.1.1 Linear stability analysis

Stability analysis plays a crucial role in assessing the performance and reliability of the system. Furthermore, in the context of the current design, stability analysis is paramount due to its direct impact on the system's efficiency, safety, and robustness. The reason being that a stable system ensures accurate tracking of the sun's position, thereby optimizing solar energy capture and maximizing energy output. Moreover, stability analysis helps identify potential instabilities that may potentially compromise the system's efficiency.

As such, to evaluate the stability of the system, two primary techniques were utilised, namely the Routh-Hurwitz and the Nyquist techniques. Additionally, a Bode plot analysis was conducted to assess the relative stability of the system. Combined, these stability analyses provide a comprehensive understanding of the systems stability.

##### 3.1.1.1 Routh-Hurwitz Stability Analysis

The Routh-Hurwitz method evaluates the stability of a system by examining the roots of its characteristic polynomial. The Routh-Hurwitz table for the given system can be seen in Table 6 below.

Table 6: Routh-Hurwitz stability analysis

$s^3$	1	182.0498	<b>0</b>
$s^2$	306.7708	95.2169	0
$s^1$	$\frac{-\begin{vmatrix} 1 & 182.0498 \\ 306.7708 & 95.2169 \end{vmatrix}}{306.7708} = 181.7394$	$\frac{-\begin{vmatrix} 1 & 0 \\ 306.7708 & 0 \end{vmatrix}}{306.7708} = 0$	$\frac{-\begin{vmatrix} 1 & 0 \\ 306.7708 & 0 \end{vmatrix}}{306.7708} = 0$
$s^0$	$\frac{-\begin{vmatrix} 306.7708 & 95.2169 \\ 181.7394 & 0 \end{vmatrix}}{306.7708} = 95.2169$	$\frac{-\begin{vmatrix} 306.7708 & 0 \\ 181.7349 & 0 \end{vmatrix}}{306.7708} = 0$	$\frac{-\begin{vmatrix} 306.7708 & 0 \\ 181.7349 & 0 \end{vmatrix}}{306.7708} = 0$

As seen in Table 6, there are no sign changes in the first column of the table. Consequently, applying the Routh-Hurwitz stability criteria, the system can be deemed to be stable. Additionally, as Table 6 contains no zero-only rows, it can be inferred that none of the poles lie on the imaginary axis.

##### 3.1.1.2 Nyquist Stability Analysis

The Nyquist analysis offers a graphical approach to stability assessment by plotting the frequency response of a system and analysing its behaviour in the frequency domain. The Nyquist plot for the given system can be seen in Figure 15 below.

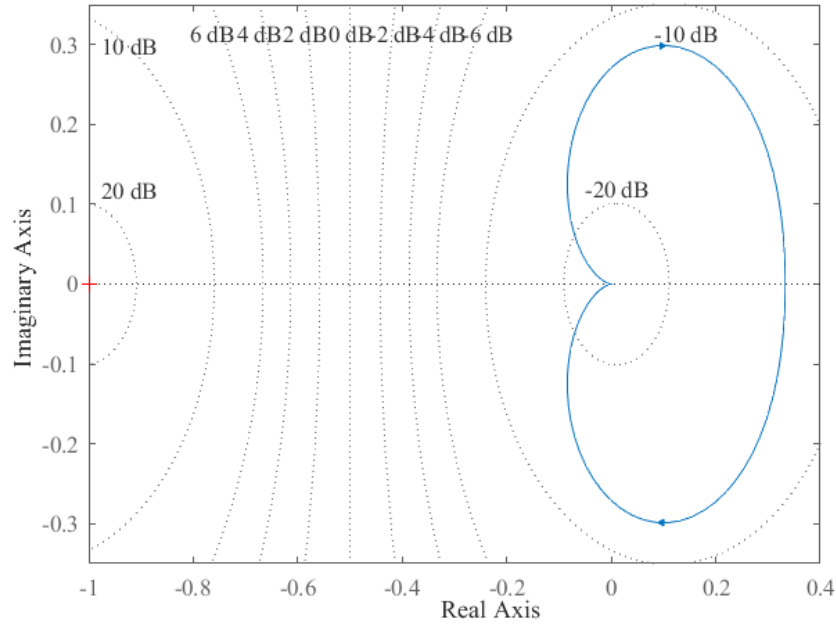


Figure 15: Linear System Nyquist Plot

As can be seen in Figure 15, the Nyquist plot does not encircle or intersect the point  $(-1, i0)$ . Therefore, in accordance with the Nyquist stability criteria, the system can be deemed stable. Thus, the results of both the Nyquist analysis and Routh-Hurwitz align with one another.

### 3.1.1.3 Analytical Validation of the Nyquist Plot

In order to validate the Nyquist Plot obtained in Section 3.1.1.2, an analytical analysis was performed on the following transfer function,

$$\frac{\theta(s)}{V(s)} = \frac{23.7894K}{s^3 + 306.7708s^2 + 182.0498s + 71.4275} \quad (3.1)$$

with no zeroes, and poles  $s_1 = -306.1770$  and  $s_{2,3} = -0.2969 \pm 0.3810i$ . Thus, it is known that the general form of the Nyquist Plot in the  $s$ -plane is as described in Figure 16:

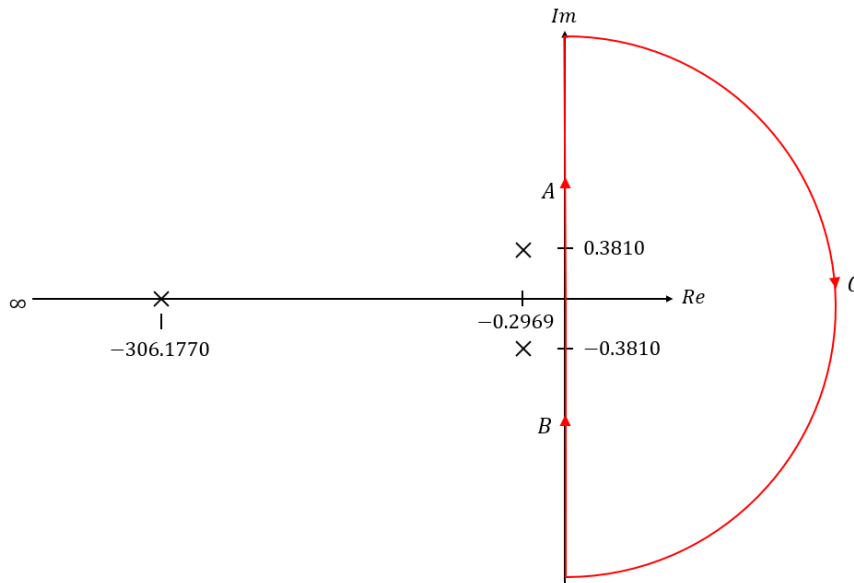


Figure 16: General form of the Nyquist Plot in the  $s$ -plane.

Furthermore, it can be seen that there are zero poles in the right-hand plane (*i.e.*  $P_{RHP} = 0$ ), with parts A, B, and C as depicted. However, this general plot now needs to be reinterpreted for the current scenario.

Thus, letting  $K = 1$

$$\frac{\theta(s)}{V(s)} = \frac{23.7894}{s^3 + 306.7708s^2 + 182.0498s + 71.4275} \quad (3.2)$$

- Reinterpreting A requires  $s = iw$ , as  $w = 0, 1, \dots, \infty$
- Reinterpreting B requires  $s = -iw$ , as  $w = -\infty, \dots, 0$  – which is the complex conjugate result of reinterpreting A
- Reinterpreting C requires  $s = Re^{i\theta}$ , as  $R \rightarrow \infty$  &  $\theta = \frac{\pi}{2}, \dots, -\frac{\pi}{2}$

As such, for Case A:

$$\frac{\theta(iw)}{V(iw)} = \frac{23.7894}{-iw^3 - 306.7708w^2 + 182.0498iw + 95.2169} \quad (3.3)$$

$$= \frac{23.7894}{(95.2169 - 306.7708w^2) + i(182.0498w - w^3)} \quad (3.4)$$

$$= \frac{23.7894}{(95.2169 - 306.7708w^2) + i(182.0498w - w^3)} \frac{(95.2169 - 306.7708w^2) - i(182.0498w - w^3)}{(95.2169 - 306.7708w^2) - i(182.0498w - w^3)} \quad (3.5)$$

$$= \frac{23.7894(95.2169 - 306.7708w^2) - i23.7894(182.0498w - w^3)}{(95.2169 - 306.7708w^2)^2 + (182.0498w - w^3)^2} \quad (3.6)$$

Separating into real (*Re*) and imaginary (*Im*) components

*Re*:

$$\frac{23.7894(94.6169 - 306.7708w^2)}{(95.2169 - 306.7708w^2)^2 + (182.0498w - w^3)^2} \quad (3.7)$$

*Im*:

$$\frac{-23.7894(94.6169 - 306.7708w^2)}{(95.2169 - 306.7708w^2)^2 + (182.0498w - w^3)^2} \quad (3.8)$$

Analysing the behaviour for Case A at points of interest:

$w = 0$ :

$$Re\left(\frac{\theta(iw)}{V(iw)}\right) = 0.2498 \quad (3.9)$$

$$Im\left(\frac{\theta(iw)}{V(iw)}\right) = 0 \quad (3.10)$$

$w = \infty$ :

$$Re\left(\frac{\theta(iw)}{V(iw)}\right) = 0 \quad (3.11)$$

$$Im\left(\frac{\theta(iw)}{V(iw)}\right) = 0 \quad (3.12)$$

$$Re\left(\frac{\theta(iw)}{V(iw)}\right) = 0:$$

$$w = 0.5571 \quad (3.13)$$

$$Im\left(\frac{\theta(iw)}{V(iw)}\right) = -0.2350 \quad (3.14)$$

$$Im\left(\frac{\theta(iw)}{V(iw)}\right) = 0:$$

$$w = 13.4926 \quad (3.15)$$

$$Re\left(\frac{\theta(iw)}{V(iw)}\right) = -0.0004267 \quad (3.16)$$

Thus, the aforementioned information can be summarised into Table 7:

Table 7: Points of interest for Case A.

<b>w</b>	0	0.5571	13.4926	$\infty$
<b>Re</b>	0.2498	0	-0.0004267	0
<b>Im</b>	0	-0.2350	0	0

Furthermore, since Case B is the reflection of Case A about the *Re* axis, the corresponding points of interest for Case B are summarised in Table 8 as follows:

Table 8: Points of interest for Case B.

<b>w</b>	0	0.5571	13.4926	$\infty$
<b>Re</b>	0.2498	0	-0.0004267	0
<b>Im</b>	0	-0.2350	0	0

For Case C:

$$\frac{\theta(Re^{i\theta})}{V(Re^{i\theta})} = \frac{23.7894}{(Re^{i\theta})^3 + 306.7708(Re^{i\theta})^2 + 182.0498(Re^{i\theta}) + 95.2169} \quad (3.17)$$

Therefore, as  $R \rightarrow \infty$

$$\frac{\theta(Re^{i\theta})}{V(Re^{i\theta})} = 0 \quad (3.18)$$

Thus, using the information obtained from reinterpreting Cases A, B, and C, the corresponding Nyquist Plot for the current scenario is plotted using Equations 3.7 and 3.8 in MATLAB, as shown in Figure 17 below:

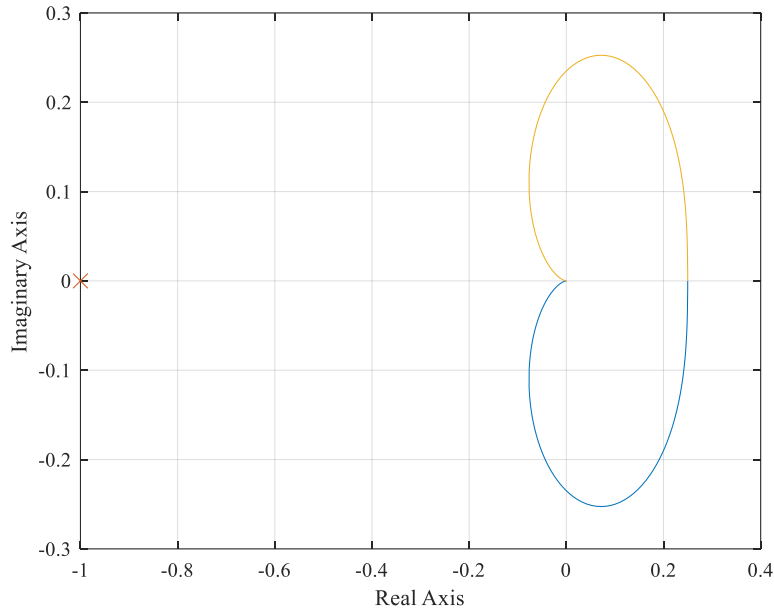


Figure 17: Analytically derived Nyquist Plot.

Furthermore, since the Nyquist Plot does not encircle the point  $s = -1$ , in either the clockwise or counterclockwise direction (*i. e.*  $N_{CCW} = 0$ ), the system can be considered stable, since

$$P_{RHP} = N_{CCW} \quad (3.19)$$

Additionally, the critical points of the Nyquist Plot, identified as points of interest, are directly proportional to the value of the gain  $K$ . By observing the effect of varying  $K$  on the point  $-0.0004267$  (which is crucial in determining whether the Nyquist Plot encircles  $-1$ ), it is evident that the system will remain stable as long as  $2344.2288 > K > 0$ . Furthermore, the requirement of  $K > 0$  arises because a negative gain value would reflect the Nyquist Plot about the imaginary axis, causing the encirclement of  $-1$  and thus the instability of the system.

#### 3.1.1.4 Bode Stability Analysis

In order to gain a greater understanding of the systems stability, a Bode Plot is required to evaluate the system's relative stability. By analysing the system's gain and phase margin, Bode analysis allows for a more comprehensive understanding of the system stability.

The Bode plot in Figure 18 below indicates that the system has a gain margin ( $GM$ ) of 67.4 dB (at a frequency of 13.5 rad/s) as well as an infinite phase margin. Consequently, these findings indicate that the system is stable in accordance with the following Bode stability criteria:

- Gain margin  $\geq 8$  dB
- Phase margin  $\geq 30^\circ$

Furthermore, it is important to note that the gain and phase margins significantly exceed the recommended stability criteria, which suggests that the system response may be sluggish. However, as the system is intended to track the position of the sun, which moves at a slow, steady rate throughout the day, the phase and gain margins are deemed to be acceptable for use in the current application.

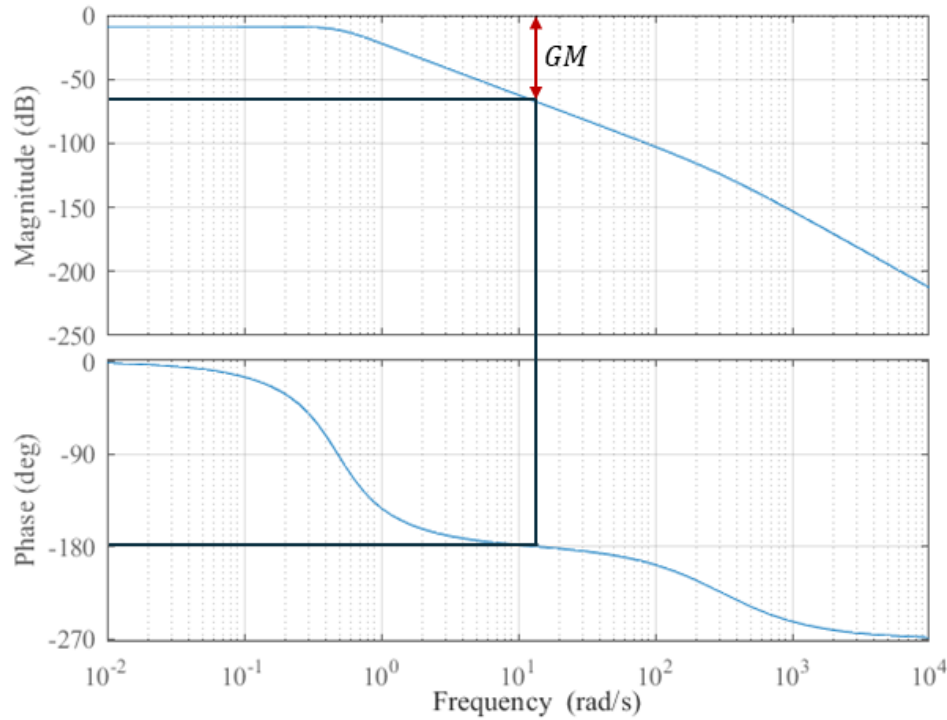


Figure 18: Linear System Bode Plot.

### 3.1.2 Non-linear stability analysis

In evaluating the stability of the nonlinear system, traditional tools used for assessing linear systems, such as the Routh-Hurwitz method, Nyquist plot, and Bode plot, are not applicable due to the inability to derive a transfer function for the nonlinear system. As such, the analysis of stability in a nonlinear system depends on employing the definition of stability, which entails assessing the system's response to disturbances or variations over time. Hence, an initial excitation (input) is imposed on the system and the response (outputs) of the system is subsequently analysed.

There are two types of stability that must be assessed for a non-linear system:

- 1) **Absolute Stability** – The system's ability to revert to its equilibrium state following any arbitrary displacement.
- 2) **Bounded Input Bounded Output (BIBO)** – The system's ability to produce a bounded response for any bounded input.



As such, to assess both stability categories the non-linear system was evaluated against two distinct input conditions, namely a pulse excitation and a sinusoidal excitation. The results from these analyses can be seen in Figure 19 below.

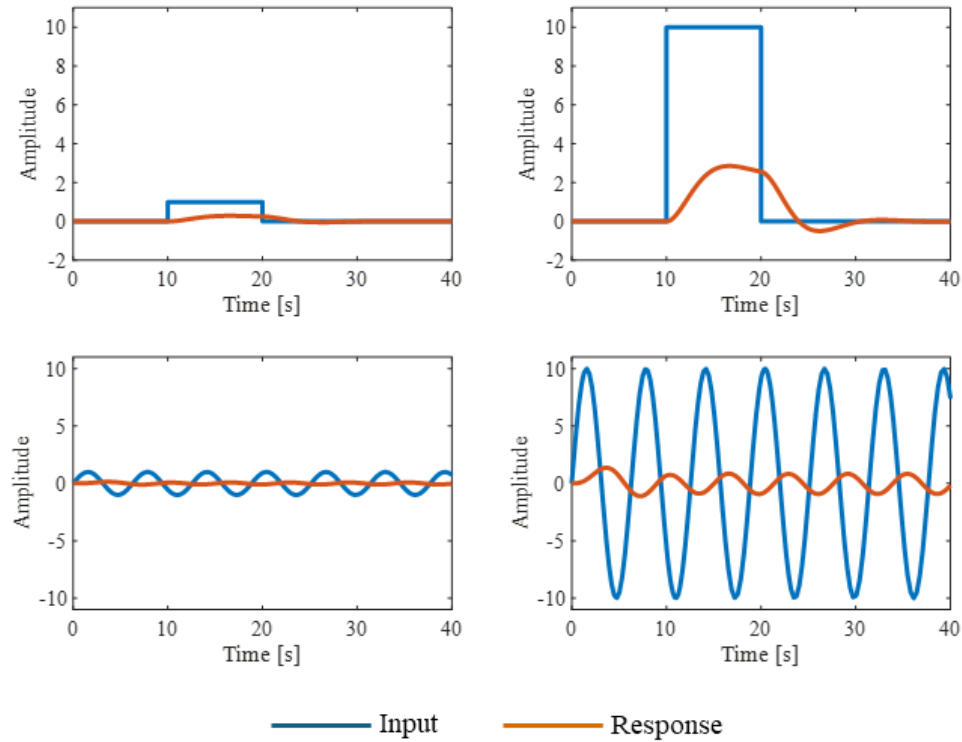


Figure 19: Non-linear system responses to various excitations.

As Figure 19 shows, when exposed to a pulse excitation, the system can return to its equilibrium condition. Moreover, when subjected to a bounded sinusoidal excitation, the system's response also remains bounded. Furthermore, both aforementioned input conditions were analysed across various input magnitudes. Subsequently, as depicted in Figure 19, the system response remains consistent under both excitations. Thus, the non-linear system is considered to exhibit both absolute stability and BIBO stability. Additionally, while the system response maintains phase coherence for both scenarios, it demonstrates a slow responsiveness, thus the system exhibits a sluggish behaviour.

### 3.1.3 Comparison of non-linear vs linear performance

In order to assess the performance of a system response, three major factors must be investigated: the system's relative stability, speed of response, and quality of response.

Furthermore, in Sections 3.1.1 and 3.1.2, the stability of the linear and non-linear systems were evaluated and deemed to be absolutely stable. Additionally, both systems displayed behavioural traits indicating that their responses may be sluggish in nature.

Moreover, as both systems are deemed stable, the remaining two behavioural factors, namely the system's speed of response and the quality of the response, can now be evaluated. As such, the following parameters relating to each system's response need to be considered:

1. **Settling time** – The duration required for a system's response to remain within a 2% tolerance band around the system steady state value.
2. **Rise time** – The time taken for a system's response to transition from 10% to 90% of the systems final steady state value.
3. **Maximum overshoot** – The peak value of a system's response curve exceeding its final steady-state value, expressed as a percentage.
4. **Stead-state error** – The difference between the desired final output and the actual output of a system when it has reached equilibrium.

Additionally, the system's speed of response is evaluated using the settling time and rise time parameters, while the quality of the response is determined using the maximum overshoot and steady-state error parameters. These parameters collectively provide a comprehensive understanding of the systems performances. Subsequently, in order to compare the performance of the linear and non-linear systems, the response of each system was evaluated after a step excitation was applied. The results of this analysis are presented in Figure 20 and Table 9 below.

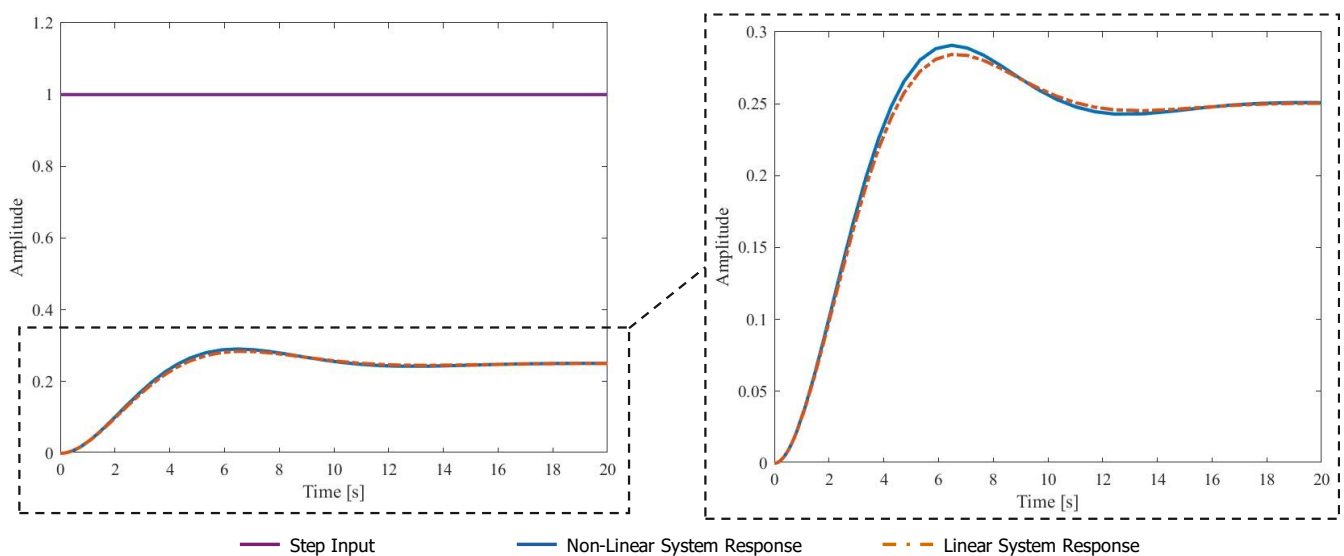


Figure 20: Comparison of Linear and Non-Linear System Step Input Response

Table 9: Comparison of performance parameters for linear and non-linear systems

	<b>Linear System Response</b>	<b>Non-Linear System Response</b>	<b>Relative Error [%]</b>
<b>Rise Time [s]</b>	3.0635	2.9249	4.74
<b>Settling Time [s]</b>	10.3832	14.5590	28.68
<b>Percent Overshoot [%]</b>	13.7823	16.3341	15.62
<b>Steady-State Error [-]</b>	0.7502	0.7502	$\approx 0$
<b>Peak Time [s]</b>	6.4814	6.4815	$\approx 0$

When examining the speed of response, it's evident that both the linear and non-linear systems initially exhibit similar behaviours, with comparable rise times and peak times. This synchronization in the early stages suggests a congruence in the initial response rates of both the linear and non-linear systems. However, the results indicate a notable disparity between the two models in terms of settling times. While the linear system stabilizes relatively quickly, the non-linear system takes longer to reach its steady state condition. This discrepancy underscores a key divergence between the linear model's prediction and the actual behaviours of the non-linear system, thus emphasizing the potential limitations of linear models in capturing complex dynamics of the real-world system accurately.

Moreover, similar disparities between the linear and non-linear systems are apparent regarding the quality of the system response. The linear system displays less overshoot compared to its non-linear counterpart, suggesting a potentially more controlled response. Additionally, both systems exhibit a steady-state error of 0.7502, indicating approximately equivalent steady-state conditions for both models.

Therefore, although some disparities exist between the linear and non-linear models, given the slow-moving nature of the solar tracker system, the impact of these differences is minimized. Consequently, the ability of the linear system to accurately model the non-linear system is deemed sufficient for the current application.

### 3.1.4 Control Implication

Given the results of the performance analysis, it is clear that the sun tracking solar panel system requires control implementation for several critical reasons. Firstly, the system response exhibits a high steady-state error. This indicates that the panels are frequently misaligned with the sun, leading to suboptimal energy absorption and reduced overall system performance. Additionally, the system is sluggish, as indicated by the slow speed of response. While this is suboptimal, due to the slow-moving nature of the sun's position, the effect of this limitation is reduced. Furthermore, the high steady-state error and sluggish response can be attributed to the high gain and phase margins inherent in the model. While

these parameters indicate that the system is stable, an overly cautious approach can result in the sluggish behaviour observed. For a sun tracking solar panel system, these issues are particularly problematic as efficient sun tracking requires a precise control system in order to maximize energy absorption throughout the day. A system plagued by high steady-state errors and slow response times fails to maintain optimal alignment with the sun, leading to significant energy losses.

Furthermore, the system needs to calculate precise gain values to convert the position error into an equivalent voltage error that drives the motor correctly. Without a control system, this precise calculation is not feasible, resulting in inefficient tracking and a thus reduced overall system performance. Moreover, without a control system, the solar panel system cannot adequately account for unexpected disturbances, such as changing wind patterns. As such, these unpredictable factors can adversely affect the orientation and stability of the solar panels, further diminishing performance. However, a robust control system can dynamically adjust to these disturbances, thus enabling the system to maintain optimal alignment with the sun and ensuring consistent energy production.

Therefore, implementing an effective control strategy is essential to mitigate these issues, ensuring the solar panels can accurately track the sun, thereby enhancing the system's efficiency and energy yield.

## 4 CONTROLLER IMPLEMENTATION

### 4.1 Closed Loop Controller Design

#### 4.1.1 Root-locus technique

The root locus method is a method that uses proportional gain control to observe the effect that the gain,  $K$ , has on the system. The plot indicates the variations of the characteristic's roots in relation to the proportional gain. This also allows us to understand what gain value will meet the system requirements. For the transfer function calculated, the root loci were plotted in MATLAB.

The pole locations give an indication of the system response, and you can design the controllers to place poles in locations which would result in the desired behaviour of the system.

##### 4.1.1.1 Analytical Calculations

$$1 + KP(s) = 0 \quad (4.1)$$

Where

$$P(s) = \frac{N(s)}{D(s)} = \frac{\theta(s)}{V(s)} \quad (4.2)$$

Where

$$\theta(s) = 23.7894 \quad (4.3)$$

And

$$V(s) = s^3 + 306.7708s^2 + 182.0498s + 71.4275 \quad (4.4)$$

##### 4.1.1.2 Roots

Zeroes:

$$N(s) = \theta(s) = 0 \quad (4.5)$$

$$\therefore \# \text{ Zeroes} = Z = 0$$

Poles:

$$D(s) = V(s) = 0 \quad (4.6)$$

$$\therefore s^3 + 306.7708s^2 + 182.0498s + 71.4275 = 0 \quad (4.7)$$

$$\therefore (s + 306.1770)(s + 0.2969 + 0.3810i)(s + 0.2969 - 0.3810i) \quad (4.8)$$

$$\therefore s_1 = -306.1170 \quad (4.9)$$

and

$$s_{2,3} = -0.2969 \pm 0.3810i \quad (4.10)$$

$$\therefore \# \text{ Poles} = P = 3$$

#### 4.1.1.3 Asymptotes

$$\theta_k = \frac{2k+1}{P-Z} 180^\circ \quad (4.11)$$

With  $k = \pm 0, \pm 1, \dots, \pm (P-Z-1)$

Therefore, since  $P-Z-1 = 3-0-1 = 2$

$$\theta_0 = \frac{2k+1}{P-Z} 180^\circ = \frac{2(0)+1}{3-0} 180^\circ = 60^\circ \quad (4.12)$$

$$\theta_1 = \frac{2k+1}{P-Z} 180^\circ = \frac{2(1)+1}{3-0} 180^\circ = 180^\circ \quad (4.13)$$

$$\theta_2 = \frac{2k+1}{P-Z} 180^\circ = \frac{2(2)+1}{3-0} 180^\circ = 300^\circ \quad (4.14)$$

#### 4.1.1.4 Asymptote Centroid

$$\sigma = \frac{\Sigma s_p - \Sigma s_z}{P-Z} \quad (4.15)$$

Where,

$$\Sigma s_p = s_1 + s_2 + \dots + s_n \quad (4.16)$$

$$\therefore \Sigma s_p = -306.1770 + (-0.2969 + 0.3810i) + (-0.2969 - 0.3810i) = -102.2569 \quad (4.17)$$

And

$$\Sigma s_z = s_1 + s_2 + \dots + s_n = 0 \quad (4.18)$$

$$\therefore \Sigma s_z = 0 \quad (4.19)$$

#### 4.1.1.5 Break Away Points

$$\frac{dK}{ds} = 0 \quad (4.20)$$

Where,

$$K = -\frac{1}{P(s)} = -\frac{D(s)}{N(s)} \quad (4.21)$$

$$\therefore K = -\frac{s^3 + 306.7708s^2 + 182.0498s + 71.4275}{23.7894} \quad (4.22)$$

Subsequently

$$\frac{dK}{ds} = 3s^2 + 613.5416s + 182.0498 = 0 \quad (4.23)$$

Resulting in

$$s = -0.2972 \quad (4.24)$$

or

$$s = -204.2167 \quad (4.25)$$

However, since none of these roots lies on the root locus, the system has no valid breakaway points.

#### 4.1.1.6 Points at which the Loci Cross the Imaginary Axis

The root locus crosses the imaginary axis when:

$$s = iw \quad (4.26)$$

But

$$D(s) + KN(s) = 0 \quad (4.27)$$

Substituting 4.26 into 4.27

$$D(iw) + KN(iw) = 0 \quad (4.28)$$

$$\therefore s^3 + 306.7708s^2 + 182.0498s + 71.4275 + 23.7894K = 0 \quad (4.29)$$

$$\therefore -iw^3 - 306.7708w^2 + 182.0498iw + 71.4275 + 23.7894K = 0 \quad (4.30)$$

Equating imaginary components and solving for  $w$

$$-w^3 + 182.0498w = 0 \quad (4.31)$$

$$w(w^2 - 182.0498) = 0 \quad (4.32)$$

$$w = 0 \quad (4.33)$$

or

$$w = \pm 13.4926 \quad (4.34)$$

Similarly equating real components and solving for  $K$

$$-306.7708w^2 + 71.4275 + 23.7894K = 0 \quad (4.35)$$

$$K = \frac{306.7708w^2 - 71.4275}{23.7894} \quad (4.36)$$

Therefore,  $w = 0$ :

$$K = -3.0025 \quad (4.37)$$

And,  $w = \pm 13.4926$ :

$$K = 2344.5852 \quad (4.38)$$

Therefore, the system will become unstable for a gain margin greater than  $K = 2344.5852$  or less than  $K = -3.0025$ .

#### 4.1.1.7 Root Locus Plot

Plotting the aforementioned information results in the following Root Locus being formed, as shown in Figure 21:

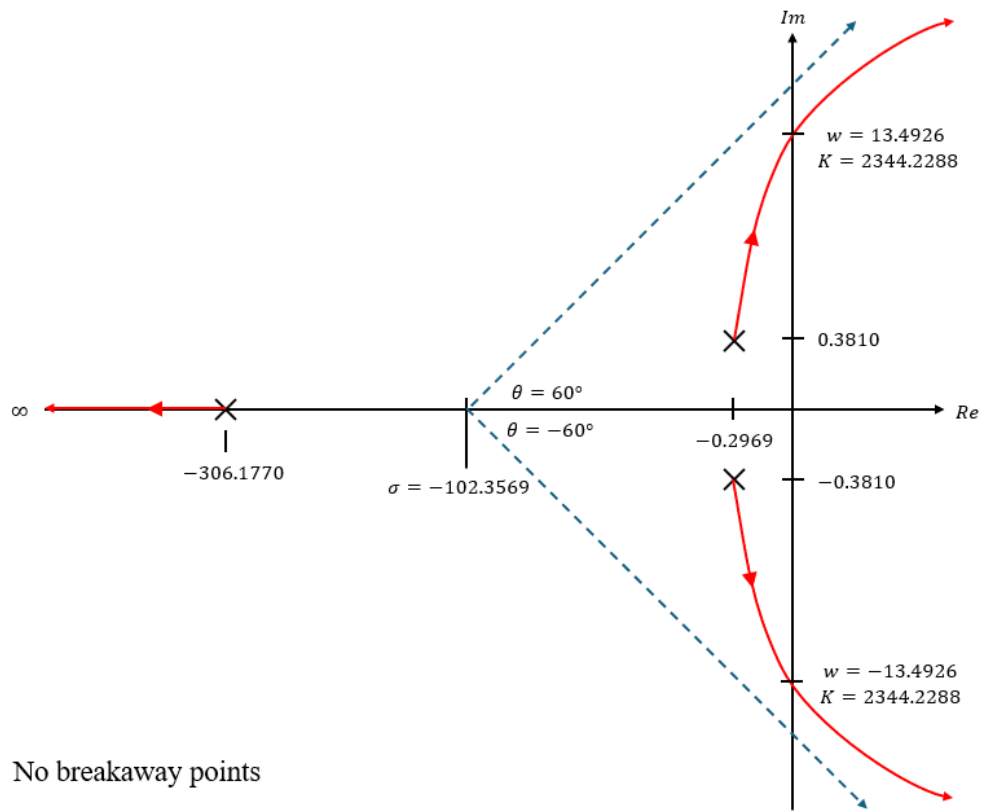


Figure 21: Diagrammatic representation of the general Root Locus behaviour.

#### 4.1.1.8 Routh-Hurwitz Stability Analysis

The statement derived in Section 4.1.1.6, can be further validated using the Routh-Hurwitz Stability Criterion, as seen in Table 10.



Table 10: Routh-Hurwitz stability analysis

$s^3$	1	182.0498	0
$s^2$	306.7708	$71.4275 + 23.7894K$	0
$s^1$	$\frac{-\begin{vmatrix} 1 & 182.0498 \\ 306.7708 & 71.4275 + 23.7894K \end{vmatrix}}{306.7708}$ $= 182.0498 - (0.2328 + 0.07755K)$	$\frac{-\begin{vmatrix} 1 & 0 \\ 306.7708 & 0 \end{vmatrix}}{306.7708} = 0$	$\frac{-\begin{vmatrix} 1 & 0 \\ 306.7708 & 0 \end{vmatrix}}{306.7708} = 0$
$s^0$	$71.4275 + 23.7894K$	0	0

Thus, for the system to be stable as per Routh-Hurwitz, the signs in the first column all need to be positive:

$s^1$ :

$$182.0498 - (0.2328 + 0.07755K) > 0 \quad (4.39)$$

$$\therefore K < \frac{182.0498 - 0.2328}{0.07755} \quad (4.40)$$

$$\therefore K < 2344.5132 \quad (4.41)$$

$s^0$ :

$$71.4275 + 23.7894K > 0 \quad (4.42)$$

$$\therefore K > -\frac{71.4275}{23.7894} \quad (4.43)$$

$$\therefore K > -3.0025 \quad (4.44)$$

The results of which agree with Section 4.1.1.6. However, when  $K < 0$ , the system will exhibit instability, as such, the system is believed to only exhibit stability for  $0 < K < 2344.5132$

#### 4.1.2 Proportional-Integral-Derivative technique

Proportional-Integral-Derivative (PID) controllers are the most common form of feedback control, typically described in the time domain by the following equation [20]:

$$u(t) = K_p e(t) + K_I \int_0^t e(\tau) d\tau + K_D \frac{de(t)}{dt} \quad (4.45)$$

where  $e(t)$  corresponds to the error signal of the system, defined as the difference between the desired setpoint and the current output of the system.

Translating to the Laplace domain, the equation becomes:

$$U(s) = K_p E(s) + K_I \frac{1}{s} E(s) + K_D s E(s) \quad (4.46)$$

where:

- $P = K_p E(s)$  produces a response that is directly proportional to the current error.
- $I = K_I \frac{1}{s} E(s)$  sums the past errors over time to produce an output proportional to the accumulated error.
- $D = K_D s E(s)$  produces an output proportional to the rate of change of the error.

Varying these parameters has different effects on the system:

- Varying  $K_p$  changes the speed of the system's response but cannot eliminate the steady-state error [21].
- Varying  $K_I$  can eliminate steady-state errors, thereby improving accuracy, but excessively high values can slow down the system response and potentially lead to instability.
- Varying  $K_D$  helps improve the speed of the response by dampening oscillations and reducing overshoot, but it is sensitive to noise in the error signal, which can cause erratic control actions [22].

To provide the best response to the error signal, most control systems typically implement all three components (P, I, and D) in a PID controller to achieve balanced control:

- $P$  provides immediate correction to the error signal.
- $I$  eliminates the steady-state error.
- $D$  dampens oscillations and reduces overshoot.

Thereby ensuring a more stable and accurate control system.

### 4.1.3 PID Tuning

The effectiveness of a PID controller relies heavily on the appropriate tuning of its gains  $K_p$ ,  $K_I$ , and  $K_D$ . Selecting the correct values for these parameters is crucial to ensure that the system's response is suitable for its intended application, as improper tuning can lead to undesirable outcomes, as shown in the Table 11 below:

Table 11: Common drawbacks of over/under tuned systems.

Tuned-Type	Drawback
<b>Under-tuned</b>	Slow response and ineffective error correction
<b>Over-tuned</b>	Instability and excessive oscillatory behaviour

Various methods exist to optimize PID gain values, such as Integral of Time-weighted Absolute Error (ITAE), Integral of Absolute Error (IAE), Integral of Squared Error (ISE), and Integral of Time Squared Error (ITSE). However, these methods require the use of a linearized system.

In contrast, MATLAB's Simulink Control Design Toolbox offers a built-in tuning tool for non-linear systems. This tool allows for real-time adjustment of parameters to achieve the desired system performance. The tuning toolbox provides two key options: selecting the desired response time and the transient behaviour of the system, summarized in the Table 12 below:

Table 12: Parameters of the Control Design Toolbox tuner

<b>Tuning Tool</b>	<b>Lower Limit</b>	<b>Upper Limit</b>
<b>Response Time</b>	Slower	Faster
<b>Transient Behaviour</b>	Aggressive	Robust

In this scenario, a faster response was desired while maintaining robustness to effectively track the azimuth angle of the sun. After tuning, the following PID values were determined to be effective for this application:

$$K_p = 61.41 \quad (4.47)$$

$$K_I = 253.5 \quad (4.48)$$

$$K_D = 409.8 \quad (4.49)$$

$$N = 13.7703 \quad (4.50)$$

Where  $N$  is the filter coefficient for the resulting system.

To ensure that the system response stayed within the motor's voltage limits, saturation constraints were applied to the PID block in the non-linear system. This resulted in upper and lower voltage limits of 27.5 V for the entire system.

#### 4.1.4 Controlled System Response Analysis

In order to evaluate the PID gains selected previously in Section 4.1.3, the response of the controlled system was analysed under three distinct input excitations: a step input, a sinusoidal input, and a ramp input. The results from this analysis are presented in Figure 22 below.

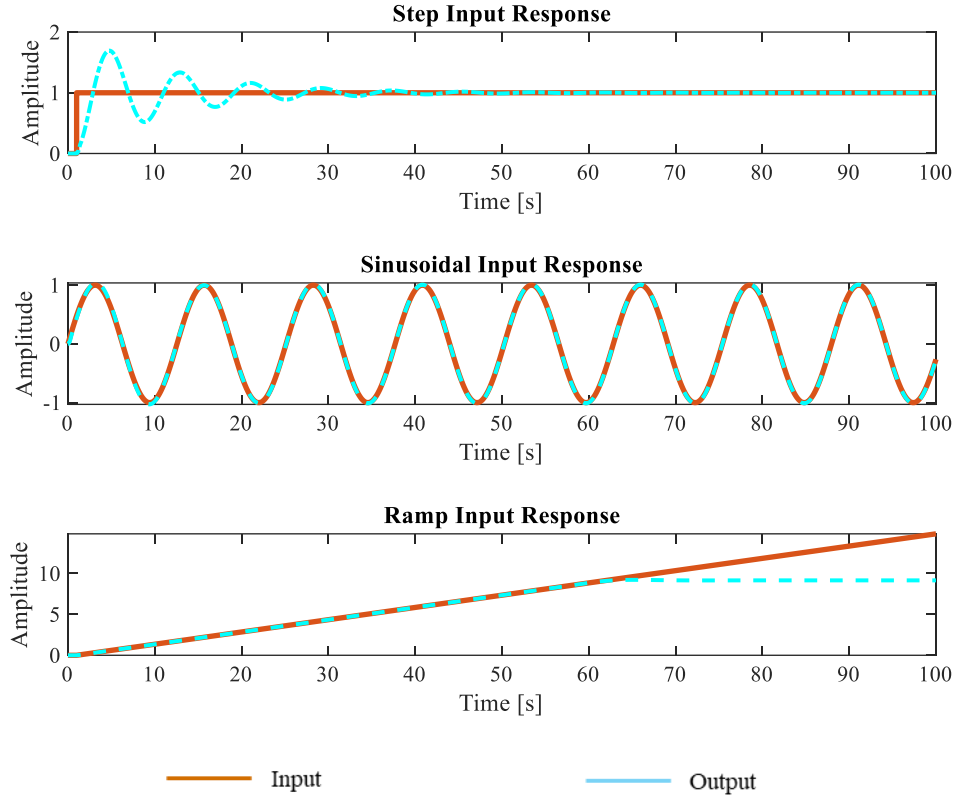


Figure 22: Controlled system's response to various input functions.

The analysis of the controlled system's response to the various input functions reveals significant insights into its performance characteristics. As illustrated in Figure 22, the PID-controlled system demonstrates a high degree of accuracy and precision when tracking sinusoidal and ramp functions. This capability indicates that the system is well-tuned to handle inputs that change gradually over time, ensuring smooth and precise adjustments that align with the expected behaviour of such inputs.

However, the system encounters difficulties when responding to the step input. This is evidenced by relatively large settling time and percentage overshoot values of 42.72s and 69.42%, respectively. These performance metrics suggest that while the PID controller excels at tracking gradually varying inputs, it struggles with sudden, large disturbances, such as those represented by a step function. Furthermore, both the peak time and the rise time for the controlled system have significantly reduced from 3.06s and 6.48s to 1.41s and 4.77s, respectively, when compared to the uncontrolled system response. This indicates that the implementation of the control system has increased the system's speed of response.

Subsequently, as the system is intended to track the relatively slow and gradual motion of the sun, it is well-suited for the given application.

Additionally, the implementation of the PID control system has significantly reduced the steady-state error that was prominent in the uncontrolled system, as detailed in Section [insert section number here]. This improvement means that the system can maintain a more accurate alignment with the sun, enhancing overall performance and energy capture efficiency.

Moreover, the analysis of the system's response to the ramp function also reveals a critical limitation: the motor's voltage limit. When the input exceeds this critical voltage value, the system is unable to continue tracking the ramp function accurately. This voltage cap is an important consideration for the design and operation of the system, as it defines the operational limits within which the system can maintain optimal performance.

## 4.2 Closed Loop Controller Application

To evaluate the effectiveness of the implemented control regime in the current scenario, the respective systems, namely the linear and non-linear systems were provided with real sun data for two specific days, as detailed in Section 2.1, specifically for the Summer and Winter Solstices, namely December 21st and June 21st.

### 4.2.1 Summer Evaluation

The control methodology's proficiency in tracking continuous changes is evident in the system's-controlled response during the summer solstice, accurately following the azimuth angle of the sun. This accuracy holds true for both the linear and non-linear systems, as they approximate the sun's trajectory. Conversely, the uncontrolled response struggles to track the sun's path, exhibiting a significant steady-state error and a sluggish reaction to changes in the azimuth angle, as can be seen in Figure 23.

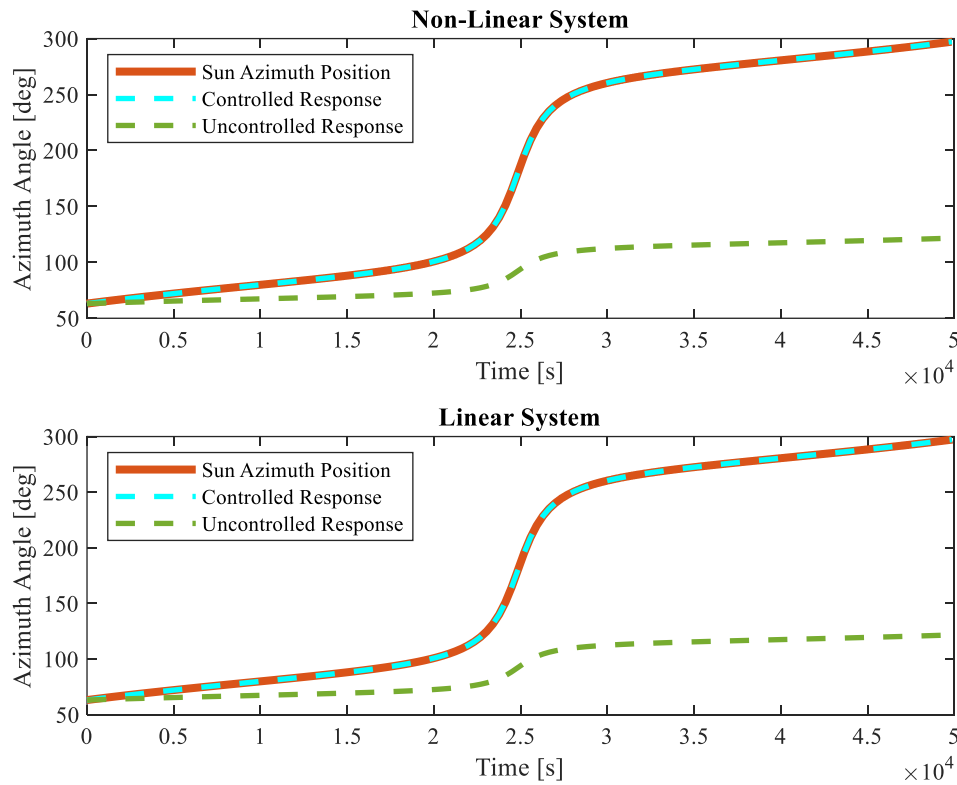


Figure 23: Comparison of solar tracking performance between the controlled and uncontrolled system for the summer solstice.

### 4.2.2 Winter Evaluation

Similarly, despite the Winter Solstice featuring shorter daylight hours, both the linear and non-linear systems exhibit comparable behaviour to that observed during the Summer Solstice. As can be seen in Figure 24, in both cases, the controlled systems effectively track the sun's azimuth angle throughout the day. However, as noted in Section 4.2.1, the uncontrolled systems exhibit the same drawbacks, including a significant steady-state error and sluggish responses. These issues are mitigated in the controlled systems through the use of large integral gains to address steady-state error and large derivative gains to counteract sluggish responses.

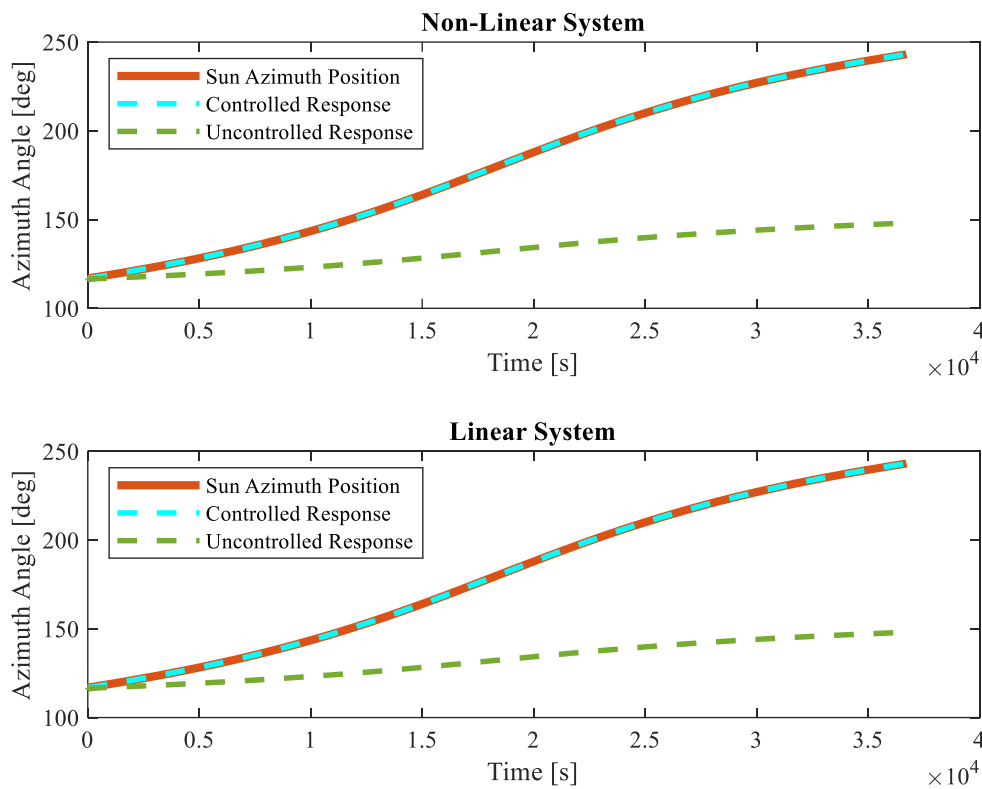


Figure 24: Comparison of solar tracking performance between the controlled and uncontrolled system for the winter solstice.

Thus, it is believed that the implementation of control within both the linear and non-linear systems result in robust systems capable of effectively tracking variations in the sun's azimuth angle across different daylight cycles. This belief is further supported by the systems' ability to accurately track the sun's trajectory during both the longest and shortest day cycles of the year.

### 4.2.3 Further System Evaluation

To evaluate the effect that large, random disturbances might have on the solar panel while it is tracking the sun—such as a large gust of wind, someone bumping into a panel, or a bird landing heavily on it—

a simulation was conducted where randomly generated disturbances were applied to the system. The response to such a disturbance is shown in Figure 25. It can be observed that the system takes approximately 60-80 seconds to recover from a significant disturbance. These disturbances are expected to be very rare, and a recovery time of around one minute is considered negligible in the overall context of the system's operation.

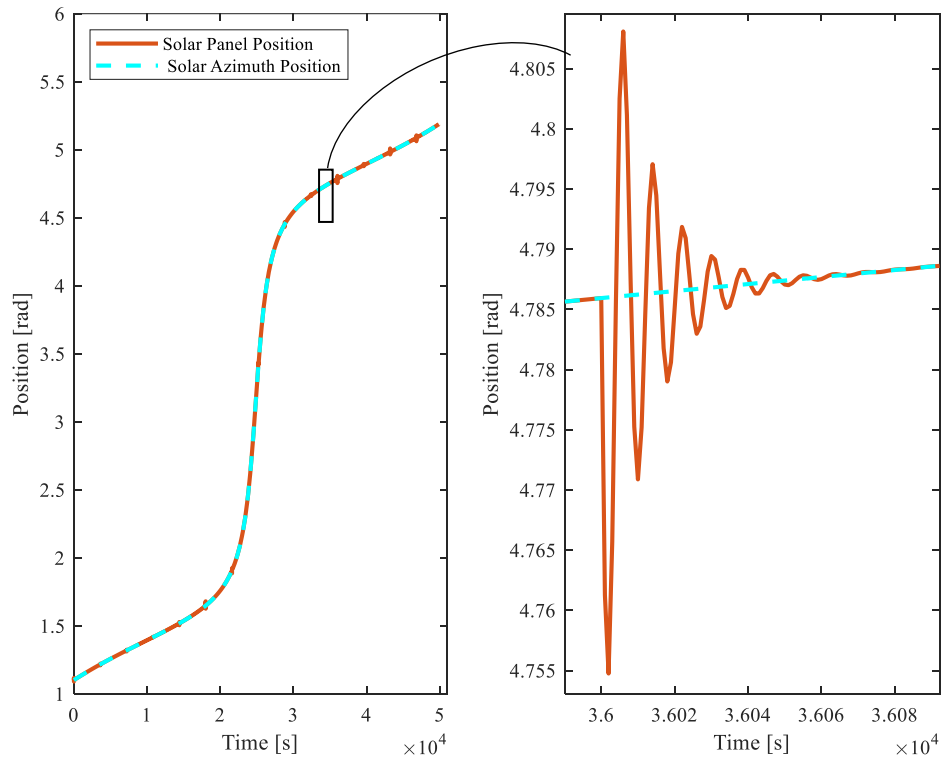


Figure 25: System response to a random disturbance.

### 4.3 Controller Performance Discussion

#### 4.3.1 Notable Results

To evaluate the feasibility of the developed solar tracker control system and determine if it meets the success criteria outlined in Section 1.2, two main aspects must be assessed: the system's physical limits and its power generation capabilities.

##### 4.3.1.1 System limits

Ensuring the modelled system operates within the physical limits is crucial for verifying that the controlled system model accurately represents the physical components. As such, the primary limitation of concern is the motor's voltage limit. Subsequently, the controller was designed with this saturation limit in mind. As confirmed by Figure 26, which displays the motor's voltage input throughout the day, the motor voltage remains within the acceptable range (below 27.5 V), thus validating the design approach. This consideration ensures the controller's commands do not exceed the motor's operational



capacity, thereby preventing potential damage and ensuring reliable performance. Additionally, the system behaves as expected as the voltage increases throughout the day. This increase is necessary for the motor to overcome the force of the torsional spring, which resists the movement of the solar panel. Thus, As the solar panel rotates further, a higher voltage is required to maintain the desired position.

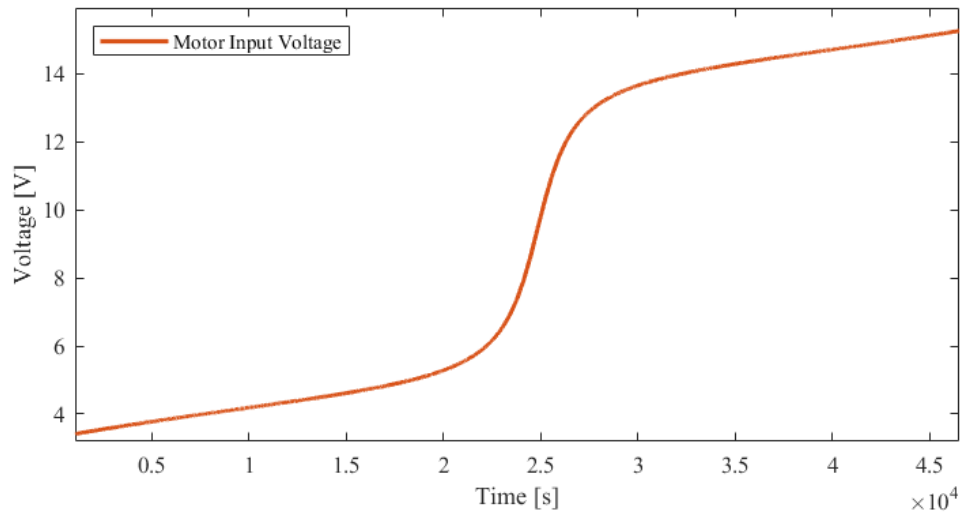


Figure 26: Daily required motor voltage input.

#### 4.3.1.2 Power generation

Determining the system's power generation capability is essential to ensure that it meets the required power output for the old age home. As such, in order to evaluate the power generated by the solar panel, the following factors must be considered.

- Solar Panel Efficiency** – Determines how well the system converts solar irradiation to power. Thus, based on the solar panel specifications, which include data on the power generated at specific irradiance levels, the solar panel's efficiency was calculated to be 22.8% [18]. Additionally, although this efficiency may vary slightly due to environmental fluctuations, for the purposes of this report, it is treated as constant.
- Solar Irradiation Variations** – The magnitude of the solar irradiation varies throughout the day. Subsequently, in order to obtain these values data was retrieved using a weather forecasting software [23], and confirmed with the results of a site assessment done for a solar park in Uppington [24]. As such, the solar irradiation values throughout the day for the summer and winter solstices can be seen in Figure 27 below, with (t=0) indicating sunrise.

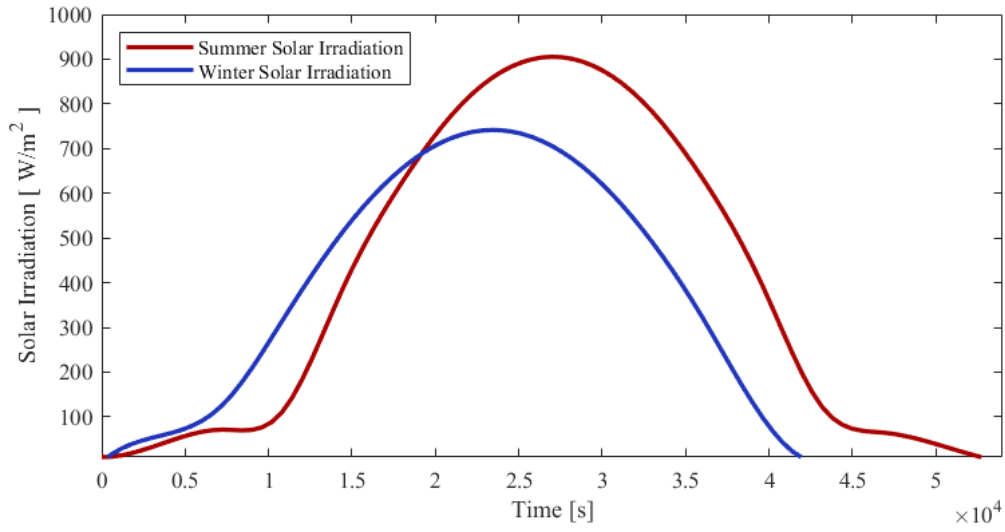


Figure 27: Change in irradiation over time for summer and winter solstices.

- **Orientation of the Sun Relative to the Panel** – In order to account for inefficiencies in the system, the component of the sun's rays perpendicular to the panel must be calculated. This component is influenced by several factors: the fixed angle of the panel, the sun's current elevation angle, the sun's azimuth angle, and the panel's tracked azimuth angle at any given time. Subsequently, this variable was calculated automatically using trigonometric relationships within the Simulink model.
- **Motor Power Usage** – The average power usage of the motor throughout the day must be calculated in order to ensure the power required by the motor does not exceed the power generated by the solar panel. Thus, the following equation was used to calculate the power required by the motor.

$$P_{avg} = \frac{V_{avg}^2}{R_a} \quad (4.51)$$

As such, accounting for these factors, the power generated by the solar panel throughout the day for the summer and winter solstices was plotted, as can be seen in Figure 28, with (t=0) indicating sunrise.

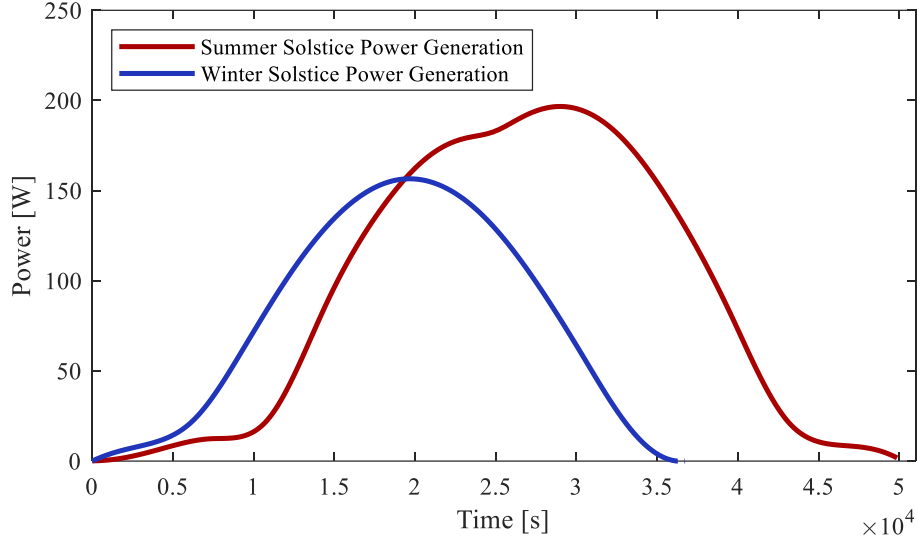


Figure 28: Solar panel power generation over summer and winter solstices.

Furthermore, by integrating the power curves in Figure 28, the total power capacity generated by the solar panel can be determined. Subsequently, as illustrated in Figure 29, the total power capacity generated per solar panel on the summer and winter solstices are 1.2689 kWh and 0.8001 kWh, respectively.

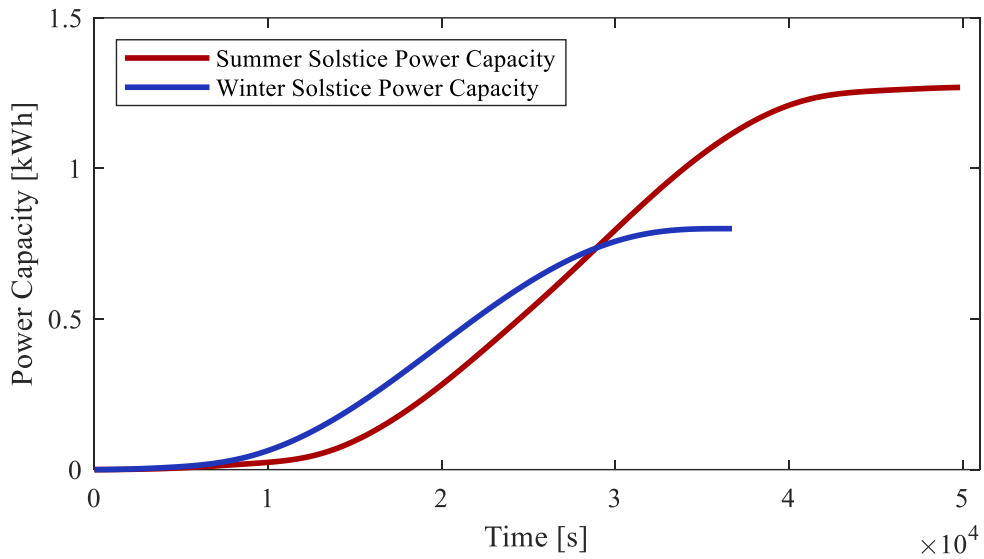


Figure 29: Cumulative power capacity of the solar panel for summer and winter solstices.

As a result, the maximum required number of solar panels can be determined using equation 4.51 below:

$$n = \text{RoundUp} \left( \frac{\text{Power Capacity Required}}{\text{Power Capacity Generated per Panel}} \right) \quad (4.52)$$

$$n = \text{RoundUp} \left( \frac{76.025}{0.8001} \right) = 114 \quad (4.53)$$

Furthermore, given that each solar panel requires a turning radius of 2.205 meters when at a fixed incline of 30°, the spatial arrangement of the panels must be optimized to fit within the designated plot of land.

Utilizing an online ‘circles within rectangles’ calculator [25], it was determined that 126 solar panels could be accommodated in each plot while maintaining a 0.5 m gap between each panel for maintenance and operational efficiency. This layout, depicted in Figure 30, ensures maximum utilization of the available space without compromising on the necessary spacing for panel rotation and efficiency.

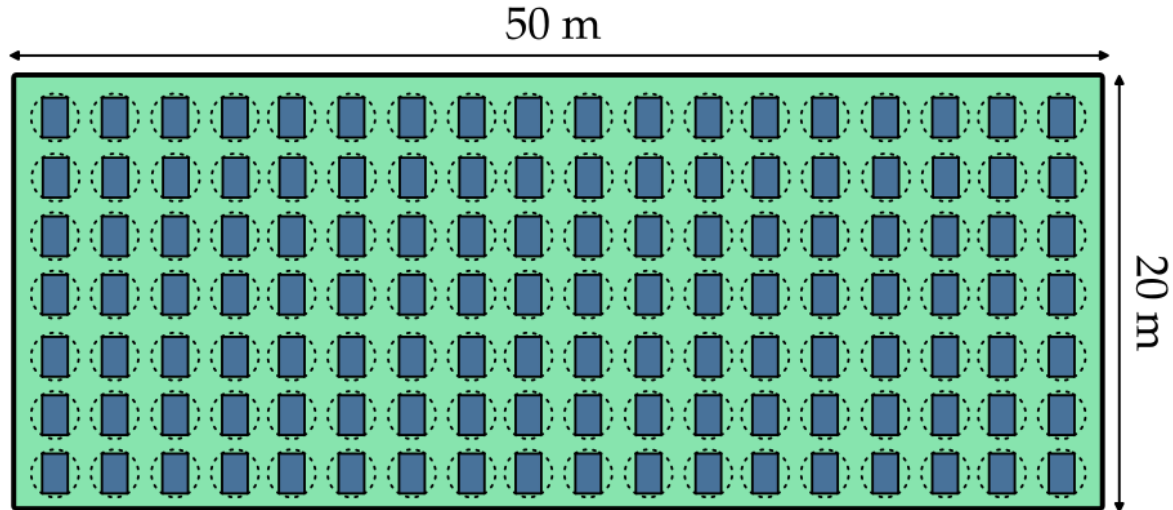


Figure 30: Solar Panel Spacing Distribution.

As such, it can be concluded that the solar tracker is able to successfully meet the power requirements of the old-age home whilst also adhering to the spacing limitations of the home.

#### 4.3.2 Model Limitations

Having established the performance of the solar panel tracking system, it is important to note the following limitations:

1. **Single Axis Control:** The current design only considers the sun’s movement along the azimuth axis. However, the sun’s position changes along both the azimuth and altitude axes throughout the day. Dual-axis tracking would be more effective in keeping the solar panels optimally aligned with the sun, thereby maximizing power generation.
2. **Space Requirements:** Due to the size of the solar panels and the power needs of each unit in the old age home, a large number of panels are required, necessitating a substantial amount of space within the home.
3. **Limited Evaluation Period:** The system was evaluated over just two days, the summer and winter solstices. While it was assumed that tracking during the longest and shortest daylight hours would be indicative of overall performance, a more comprehensive assessment should include multiple days within a month and across different months. This would provide a better understanding of the system’s performance under various conditions.
4. **Unmodeled Weather Conditions:** The model included wind disturbances but did not account for other environmental factors such as mist, dust, and clouds. These conditions can impact the

system's ability to track the sun and generate the required power. The effects of persistent adverse weather on the power supply for the retirement village thus remain unknown.

#### **4.4 Necessary Instrumentation**

In order to successfully implement the control system within the solar tracking design, the following instrumentation is necessary [26, 27]:

1. Control Unit:

- The control unit executes the solar tracking algorithm and controls the motion of solar panels along the azimuth axis. It processes sensor inputs, generates control signals, and commands actuators to adjust panel orientation for optimal sun tracking.

2. Encoders/IMU (Inertial Measurement Unit):

- Encoders or IMUs measure the angular position of mechanical components, providing feedback to the solar tracking algorithm for precise panel movement along the azimuth axis. This ensures accurate sun tracking throughout the day.

3. Worm Gears:

- Worm gears transmit motion between perpendicular shafts, converting motor rotation into angular movement of the solar panel along the azimuth axis. Their high gear reduction ratios and self-locking characteristics enable precise and stable motion control.

4. Torsional Spring:

- A torsional spring returns the solar panel to its sunrise position upon sunset, ensuring effective and reliable solar tracking by maintaining the desired orientation.

5. Photodetector:

- Photodetectors detect sunlight intensity and direction, providing feedback for optimal solar tracking along the azimuth axis. They enhance system responsiveness by continuously adjusting panel orientation to maximize sunlight exposure.

6. Limit Switches:

- Limit switches are electromechanical devices used to restrict physical motion. Placed at the azimuth axis's maximum endpoints, they signal when the solar panel reaches its maximum allowed position, indicating sunset and preventing overtravel.

Furthermore, if the system were to be made more robust, such as through the use of dual-axis solar tracking, additional instrumentation would include:

7. Anemometer:

- Measures wind speed to safeguard against strong winds by driving the panels to a safe position until wind conditions subside, preventing potential damage.

8. Inclinator:

- Also known as a tilt sensor, it ensures accurate sun tracking about the altitude angle by providing feedback on the sun's position in the sky. This assists in maintaining optimal tilt angles for precise solar tracking.

## 5 CONCLUSION

As required, a solar tracker was designed and developed to follow the sun's azimuth position throughout the day. Due to the sluggish response of the uncontrolled plant, a control system was required to meet the system requirements. Furthermore, the control system needed to be optimised for tracking slow, steady movements, whilst still maintaining the capability to stabilise the system after a disturbance. Subsequently, the performance of the tracker was deemed to be suitable due to its relatively quick stabilisation period (compared to the time period of a day), and excellent tracking capabilities.

Moreover, in order to satisfy the required success criteria, as defined in section 1.2, the system needed to both:

- Fit within the designated solar farm area.
- Generate more than 25% of the daily electricity usage of the old age home.

Since the available plot of land had enough space to comfortably fit 126 solar panels, and only 114 panels are required during the shortest day, both success criteria were satisfied, and thus the sun tracker system is deemed successful.

The final system specifications are thus as follows:

Table 13: Final system specifications.

Power Specifications		
# Solar Panels Required	114	
Winter		
Power Yield per Panel	0.8	kWh
Total Power Yield	76.6764	kWh
Summer		
Power Yield per Panel	1.2689	kWh
Total Power Yield	125.0513	kWh
PID Values		
$K_P$	61.41	
$K_I$	253.5	
$K_D$	409.8	
$N$	13.7703	
Stable	Yes	

## 6 REFERENCES

- [1] Anonymous, “South Africa’s solar boom against load shedding,” IOL, 3 October 2023. [Online]. Available: <https://www.iol.co.za/business-report/opinion/south-africas-solar-boom-against-load-shedding-d9e5a051-bc94-4a06-9dff-b4dcb21cf58a>. [Accessed 11 May 2024].
- [2] Anonymous, “How does load shedding affect people’s lives,” ELSS, 13 February 2023. [Online]. Available: <https://eskomloadsheddingschedule.co.za/how-does-load-shedding-affect-peoples-lives/#:~:text=Load%20shedding%2C%20or%20planned%20power%20outages%2C%20is%20a,to%20loss%20of%20income%20and%20quality%20of%20life..> [Accessed 11 May 2024].
- [3] “It’s time to dump Eskom and your generator, and fall in love with solar,” Sectional Title Solutions, 24 February 2022. [Online]. Available: <https://www.stsolutions.co.za/dump-eskom-and-your-generator-and-fall-in-love-with-solar/>. [Accessed 11 May 2024].
- [4] T. A. A. S. K. R. WK Ahmed, “Environmental impact of using generators,” *Journal of Thermal*, 2020.
- [5] T. P. a. C. O. S. E. (. Guide), Forbes Home, [Online]. Available: <https://www.forbes.com/home-improvement/solar/solar-energy-pros-and-cons/>. [Accessed 11 May 2024].
- [6] GES Green Energy Solutions, “Cost of solar panels,” 2024. [Online]. Available: <https://greenenergysolutions.co.za/current-state-of-solar-in-south-africa/>. [Accessed 11 May 2024].
- [7] A. A.-O. F. K. M Tawalbeh, “Environmental impacts of solar photovoltaic systems: A critical review of recent progress and future outlook,” *Elsevier*, 2021.
- [8] t. a. a. Solar trackers: What they are, Repsol, [Online]. Available: <https://www.repsol.com/en/energy-and-the-future/future-of-the-world/solar-trackers/index.cshtml>. [Accessed 10 May 2024].
- [9] T. Giordano, “South African Renewable Energy Resource Database-annual solar radiation,” Research Gate, 2024. [Online]. Available: [https://www.researchgate.net/figure/South-African-Renewable-Energy-Resource-Database-annual-solar-radiation\\_fig5\\_265206846](https://www.researchgate.net/figure/South-African-Renewable-Energy-Resource-Database-annual-solar-radiation_fig5_265206846). [Accessed 18 May 2024].



- [10] “Exploring the perceptions of old age (home) residents regarding the general care received (by the elderly) in the O.R. Tambo District Eastern Cape,” [Online]. Available: <https://researchspace.ukzn.ac.za/items/5498b007-4091-4f8c-b5f8-c8d29e4>. [Accessed 11 May 2024].
- [11] “Power plant profile: Upington Solar PV Park, South Africa,” [Online]. Available: <https://www.power-technology.com/data-insights/power-plant-profile-upington-solar-pv-park-south-africa/>. [Accessed 10 May 2024].
- [12] N. Maina, “Azimuth angle in solar PV systems,” LinkedIn, 2023. [Online]. Available: [https://www.linkedin.com/posts/neliusmaina24\\_azimuth-angle-in-solar-pv-systems-the-azimuth-activity-7126495277573636097-Tw\\_-/](https://www.linkedin.com/posts/neliusmaina24_azimuth-angle-in-solar-pv-systems-the-azimuth-activity-7126495277573636097-Tw_-/). [Accessed 10 May 2024].
- [13] A. Brooks and L. Saddler, “What Is The Best Angle And Orientation For Solar Panels?,” Forbes Home, 7 March 2024. [Online]. Available: <https://www.forbes.com/home-improvement/solar/best-angle-for-solar-panels/#:~:text=This%20is%20done%20by%20tilting,30%20degrees%20and%2045%20degrees..> [Accessed 21 April 2024].
- [14] Wind Finder, “Annual wind and weather statistics for Upington Airport,” Wind Finder, 2024. [Online]. Available: [https://www.windfinder.com/windstatistics/upington\\_airport](https://www.windfinder.com/windstatistics/upington_airport). [Accessed 20 April 2024].
- [15] trojanfans, “Altitude & Density Chart,” trojanfans, 2024. [Online]. Available: <http://www.trojanfans.com/altidens.htm>. [Accessed 5 May 2024].
- [16] latitudelongitude.org, “Upington, South Africa latitude longitude,” latitudelongitude.org, 2024. [Online]. Available: <https://latitudelongitude.org/za/upington/>. [Accessed 21 April 2024].
- [17] S. F. Hoerner, Fluid-Dynamic Drag, Washington: Walter S. Diehl, 1963.
- [18] Sankopower, “Mono Solar Panel Catalogue,” [Online]. Available: <https://www.sankopower.com/pdf/Mono-Solar-Panel-Catalogue.pdf>. [Accessed 2 April 2024].
- [19] Moog Inc., “DB-4000 MATRIX SERIES SPECIFICATIONS,” 2024. [Online]. Available: <https://www.moog.com/content/dam/moog/literature/MCG/DB-4000.pdf>. [Accessed 28 April 2024].
- [20] I. Parnell, “What is PID control?,” 30 January 2014. [Online]. [Accessed 10 May 2024].

- [21] ni, "PID Theory Explained," ni," 2020 March 17. [Online]. Available: <https://www.ni.com/en-za/innovations/white-papers/06/pid-theory-explained.html#section--2132865782>. [Accessed 10 05 2024].
- [22] D. Collins, "FAQ: What are PID gains and feed-forward gains?, Motion Controp tips, 30," 30 December 2016. [Online]. Available: <https://www.motioncontroltips.com/faq-what-are-pid-gains-and-feed-forward-gains/>. [Accessed 10 May 2024].
- [23] TuTiempo, "Solar radiation in Upington," TuTiempo, 2024. [Online]. Available: <https://en.tutiempo.net/solar-radiation/upington.html>. [Accessed 17 May 2024].
- [24] GeoModel Solar, "Upington Solar Park," GeoModel Solar, 14 June 2011. [Online]. Available: [https://www.crses.sun.ac.za/files/research/publications/technical-reports/GeoModelSolar\\_SolarResRep\\_58-01-2011\\_Upington\\_rev2.pdf](https://www.crses.sun.ac.za/files/research/publications/technical-reports/GeoModelSolar_SolarResRep_58-01-2011_Upington_rev2.pdf). [Accessed 17 May 2024].
- [25] The Engineering ToolBox, "Circles within a Rectangle - Calculator," The Engineering ToolBox, 2014. [Online]. Available: [https://www.engineeringtoolbox.com/circles-within-rectangle-d\\_1905.html](https://www.engineeringtoolbox.com/circles-within-rectangle-d_1905.html). [Accessed 18 May 2024].
- [26] Penn State, "Engineered devices for solar tracking," Penn State, 2024. [Online]. Available: <https://www.e-education.psu.edu/eme812/node/585>. [Accessed 17 May 2024].
- [27] Solarmems, "Solar Tracking," Solarmems, 2024. [Online]. Available: <https://solar-mems.com/solar-tracking/#:~:text=ISS%2DDX%20Sun%20Sensor%3A%20A,along%20with%20the%20solar%20radiation>. [Accessed 17 May 2024].
- [28] D. S. P. W. o. C. Days?, Solar Alliance, [Online]. Available: <https://www.solaralliance.com/how-do-clouds-affect-solar-panels/>. [Accessed 10 May 2024].
- [29] H. m. e. d. s. p. p. f. y. home, YES Energy Solutions, [Online]. Available: <https://www.yesenergysolutions.co.uk/advice/how-much-energy-solar-panels-produce-home>. [Accessed 11 May 2024].

## **7 APPENDICIES**

### **7.1 Appendix A – Relevant Code Used**

\*Please refer to the attached zipped folder for the relevant code files used within the current report\*